Numerical homogenization of the viscoplastic behavior of snow based on X-ray tomography images

Antoine Wautier[1,2,3,4,5], Christian Geindreau[1], and Frédéric Flin[2]

[1]Université Grenoble Alpes, CNRS, Grenoble INP, Laboratoire 3SR UMR5521, F-38000 Grenoble, France
[2]Météo-France – CNRS, CNRM UMR 3589, CEN, F-38400 Saint Martin d'Hères, France
[3]Now at AgroParisTech-ENGREF, 19 avenue du Maine, 75732 Paris, France.
[4]Now at Irstea UR RECOVER, 3275 Rte Cézanne, CS 40061, 13182 Aix-en-Provence Cedex 5, France.
[5]Now at Université Grenoble Alpes, Irstea, UR ETGR, 2 rue de la Papeterie-BP 76, F-38402 St-Martin-d'Hères, France.

Correspondence to: A. Wautier (antoine.wautier@gmail.com)

Abstract. The homogenization techniques recently developed for the numerical study of the elastic behavior of snow are adapted to its non-linear visco-plastic behavior. Based on the definition of kinematically uniform boundary conditions, homogenization problems are applied to 3D-images obtained by X-ray tomography, and the mechanical response of snow samples of different densities is explored. An original post-processing approach in terms of viscous dissipated powers is defined in order to formulate the macroscopic behavior of snow. Then, the ability of Abouaf models to account for snow visco-plastic behavior is shown and a homogenized constitutive equation is proposed based on a density parametrization. Finally, the mechanical responses of snow for classical laboratory tests are analyzed and compared with the proposed model.

1 Introduction

It is now well known that the macroscopic mechanical behavior of snow strongly depends on its microstructure, which is mainly characterized by its density (Mellor, 1974) and its topology (Shapiro et al., 1997), by the mechanical behavior of the ice matrix (elastic, visco-plastic, brittle-failure) depending on the external load, by the temperature (Schweizer and Camponovo, 2002) and by the applied strain rate (Schulson et al., 2009). For example, at high strain rate, large deformations of snow are mainly controlled by grain rearrangements resulting from the failure of cohesive bonds, whereas at very low strain rates ($< 10^{-5}\mathrm{s}^{-1}$ typically), snow exhibits a visco-plastic behavior (Narita, 1984; Salm, 1982) which plays an important role in the long-term densification of the snowpack. In practice, a good knowledge of the macroscopic mechanical behavior of snow in a wide range of applied loads, strain rates and temperatures is of a particular interest with respect to avalanche risk forecasting or to determine the forces on avalanche defense structures.

During the last decades, numerous experimental studies have been performed in order to characterize the macroscopic behavior of different types of snow under various loading conditions and temperatures (Mellor, 1974; Salm, 1982; Desrues et al., 1980; Shapiro et al., 1997; Bartelt and von Moos, 2000; Moos et al., 2003; Scopozza and Bartelt, 2003a). In the framework of the continuum mechanics, several models have been then proposed in order to reflect these experimental data (Desrues et al.,

1980; Scopozza and Bartelt, 2003b; Cresseri and Jommi, 2005; Navarre et al., 2007; Cresseri et al., 2009). However, the fitted material parameters arising in these models often characterize the mean properties of a few types of snow in a restricted density range. Thanks to the recent application of X-ray tomography to snow (Brzoska et al., 1999; Schneebeli, 2004; Kaempfer et al., 2005; Flin and Brzoska, 2008; Chen and Baker, 2010; Srivastava et al., 2010; Pinzer et al., 2012; Wang and Baker, 2013; Adams and Walters, 2014; Calonne et al., 2015) good databases of 3D images for the different snow types described in the international classification (Fierz et al., 2009) are now available (Calonne et al., 2012; Löwe et al., 2013). Given these extensive geometrical descriptions of snow, its corresponding macroscopic behavior can be up-scaled in a more systematic way thanks to the use of techniques derived from the homogenization theory (Dormieux and Bourgeois, 2002; Auriault et al., 2010).

In recent works, the combination of X-ray tomography imaging, finite element techniques (FEM) or discrete element methods (DEM) and ever increasing computing power was used to bridge the gap between the topology of the ice skeleton of snow and its mechanical behavior.

- In the FEM method, the complex 3D snow skeleton observed by X-ray microtomography can be meshed without loosing any information on the microstructure and different mechanical behaviors of the polycrystalline ice can be considered. In the last decade, most of the studies were dedicated to the elastic behavior of snow (Schneebeli, 2004; Pieritz et al., 2004; Srivastava et al., 2010; Köchle and Schneebeli, 2014; Wautier et al., 2015; Srivastava et al., 2016), possibly up to a brittle failure (Hagenmuller et al., 2014). Concerning the modeling of more complex snow constitutive behaviors, the proposed approaches mainly focus on the modeling of uniaxial compression tests. For instance, Theile et al. (2011) has proposed a beam network model based on 3D images to simulate creep of snow whereas Chandel et al. (2014) used an elasto-plastic constitutive law for ice in order to determine the failure envelope.

- In the DEM method, the snow skeleton is viewed as an assemblage of ice grains interacting between each other through contact points. This method is well suited to model complex interactions taking place at the interface between snow grains such as elasto-viscoplastic contact deformation, grain sintering and bond breakage or sliding possibly leading to grains rearrangement. It has been already used on 3D idealized assemblages of ice grains (Johnson and Hopkins, 2005) to identify microstructural deformation mechanisms of snow and to simulate creep densification process. The application of the DEM directly on images obtained by X-ray tomography is not straightforward, since every ice grain constituting the skeleton must be identified. Recently, DEM simulations taking into account cohesion and friction at the contact between grains have been performed on more realistic 3D assemblages of grains deduced from X-tomography (Hagenmuller et al., 2015). However the shape of each ice grain is approximated by a clump of spheres. Moreover, all these simulations have been performed without taking into account the crystalline orientation of each ice grain. These orientations can play an important role on the viscous deformation mechanisms (secondary creep) at the contact between two grains as it has been recently shown by Burr et al. (2015b, a). The granular structure of snow (grain shape and crystal orientations) can be determined on real 3D images of snow by X-ray Diffraction Contrast Tomography (DCT)

(Rolland du Roscoat et al., 2011). However the application of this technique is not straightforward and very few images are now available.

In the following, we propose to formulate a 3D macroscopic viscoplastic constitutive law for snow by performing FEM simulations on 3D images, which is of particular interest while considering the long term densification of the snowpack under its own weight. During this process, snow deforms at a low strain rate and an important part of the densification results from the viscous deformation (secondary creep) of the ice skeleton. As performed in Wautier et al. (2015) within the framework of elasticity, typical kinematically uniform boundary conditions (KUBC) are applied to 3D images of snow, and finite element simulations are run in order to link the macroscopic stress response of different snow samples to imposed strain rates in an incremental form. Indeed, for each numerical simulation, only small strains are considered to avoid any important microstructure modification. Then, the macroscopic law is generalized to finite deformation problems thanks to the use of a collection of 3D snow images exhibiting different microstructures and densities. In this upscaling process, the viscous behavior of ice is described by a power law of exponent n (secondary creep) as in Theile et al. (2011). Due to the non-linear behavior under consideration, the homogenization does not provide the complete structure of the macroscopic constitutive equation (Auriault et al., 1992, 2002; Geindreau and Auriault, 1999; Orgéas et al., 2007). However, it can be shown that the exponent n is preserved at the macroscopic scale and that the macroscopic dissipation potential is the volume-averaged of the local dissipation one (Suquet, 1993). Using these properties, the macroscopic constitutive equation of snow can be formulated within the framework defined by the theory of representation of anisotropic tensor functions (Smith, 1971; Liu, 1982) and by using macroscopic isodissipation surfaces (Green, 1972; Abouaf, 1985; Duva and Crow, 1992; Sofronis and McMeecking, 1992; Geindreau et al., 1999b; Storakers et al., 1999; Sanchez et al., 2002; Orgéas et al., 2007).

The paper is organized as follows. In section 2, the numerical homogenization procedure used in Wautier et al. (2015) is recalled and adapted to the study of a non-linear constitutive equation. Section 3 presents the post-processing procedure that was used in order to characterize the macroscopic viscous behavior of snow in terms of macroscopic isodissipation curves. These curves might be seen as the equivalent of yield surfaces in plasticity as they characterize the set of stress or strain rate states leading to the same level of mechanical dissipation. Their shape and size, which results from the strong coupling between the microstructure of the ice skeleton and the ice viscous behavior at the microscale, characterizes the 3D viscoplastic behavior of snow. In section 4, the obtained numerical results for snow samples of different densities are presented and the ability of an Abouaf's model (Abouaf, 1985) to describe the macroscopic viscous behavior of snow is highlighted. In the end of this section, a macroscopic formulation of the viscoplastic behavior of ice is formulated. Finally, in section 5, the mechanical responses of snow for classical experimental tests (uniaxial, oedometric and triaxial compression tests) are modeled thanks to the upscaled laws. This illustrates the potential applications of the proposed 3D homogenized constitutive behavior.

2   Numerical homogenization procedure: from image to macroscopic mechanical response

Based on the homogenization theory, it is often possible to replace a heterogeneous material by an equivalent homogeneous one provided that its microstructure is sufficiently small with respect to the macroscopic scale of interest. With respect to snow, this separation of scale hypothesis is satisfied in most of the cases and its macroscopic mechanical behavior can be deduced from mesovolumes obtained thanks to X-ray tomography. Previous studies showed that in most of the cases, samples of a few millimeters can be considered as representative elementary volumes (REV) for the study of the mechanical behavior of snow (Wautier et al., 2015; Srivastava et al., 2016). In the following, in order to distinguish the two scales of interest, lowercase letters are used for microscopic quantities whereas uppercase letters are used for their macrosccopic counterparts.

Irrespective of the size of the sample considered, the boundary conditions used in a homogenization procedure introduce undesired boundary effects of varying thickness. Depending on the type of boundary conditions used, the size of the REV should be adapted accordingly. Three particular types of boundary conditions are considered to give relatively small REV. In decreasing order of REV (Kanit et al., 2003), these are statically uniform boundary conditions (SUBC), with a macroscopic homogeneous stress imposed on the boundary, kinematically uniform boundary conditions (KUBC), with a macroscopic homogeneous strain imposed on the boundary, and periodic boundary conditions (PBC), with a periodicity condition imposed on the displacement field and the normal stress across the sample boundaries. Although PBC are considered to give the best convergence with respect to the size of the REV (Kanit et al., 2003), their application to a non-periodic highly porous microstructure is not straightforward. It is necessary, for example, to enclose the sample by a virtual boundary or assume that the pores are filled by a soft material. In order to avoid the introduction of such artifacts, KUBC were retained. The KUBC numerical homogenization procedure introduced in Wautier et al. (2015) is used in this paper and easily adapted to the study of the elasto-viscoplastic behavior of snow. It consists in the four steps recalled in Figure 1.

The first two steps remain unchanged and consist in: (i) meshing of 3D-microtomographic images (Step 1), (ii) defining the kinematic relation $\boldsymbol{u} = \mathbf{E} \cdot \boldsymbol{x}$ between the homogeneous macroscopic strain $\mathbf{E}$ and the displacement field $\boldsymbol{u}$ on the boundary (Step 2). Step 1 requires the use of the MATLAB open-source toolbox iso2mesh (Fang and Boas, 2009) while step 2 is achieved thanks to the use of the plug-in Homtools (Lejeunes et al., 2011). More details can be found in Wautier et al. (2015). The next two steps (Step 3 and Step 4) are modified in order to take into account the change in the constitutive modeling of ice.

2.1   Elasto-viscoplastic behavior of ice (Step 3)

In the following, the mechanical behavior of the polycrystalline ice is supposed to be elasto-viscoplastic and isotropic. The total strain rate tensor ($\dot{\boldsymbol{\varepsilon}}$) is decomposed as the sum of the elastic part ($\dot{\boldsymbol{\varepsilon}}_e$) and a viscous part ($\dot{\boldsymbol{\varepsilon}}_v$) as

$$\dot{\boldsymbol{\varepsilon}} = \dot{\boldsymbol{\varepsilon}}_e + \dot{\boldsymbol{\varepsilon}}_v. \tag{1}$$

The elastic part can be expressed as, $\boldsymbol{\varepsilon}_e = (\mathbf{C}^{\mathrm{ice}})^{-1} : \boldsymbol{\sigma}$, where $\mathbf{C}^{\mathrm{ice}}$ is the elastic stiffness tensor, $\boldsymbol{\sigma}$ is the Cauchy stress tensor and ":" the double contraction product. Due to isotropy, $\mathbf{C}^{\mathrm{ice}}$ is fully defined by a Young's modulus E and a Poisson ratio ν.
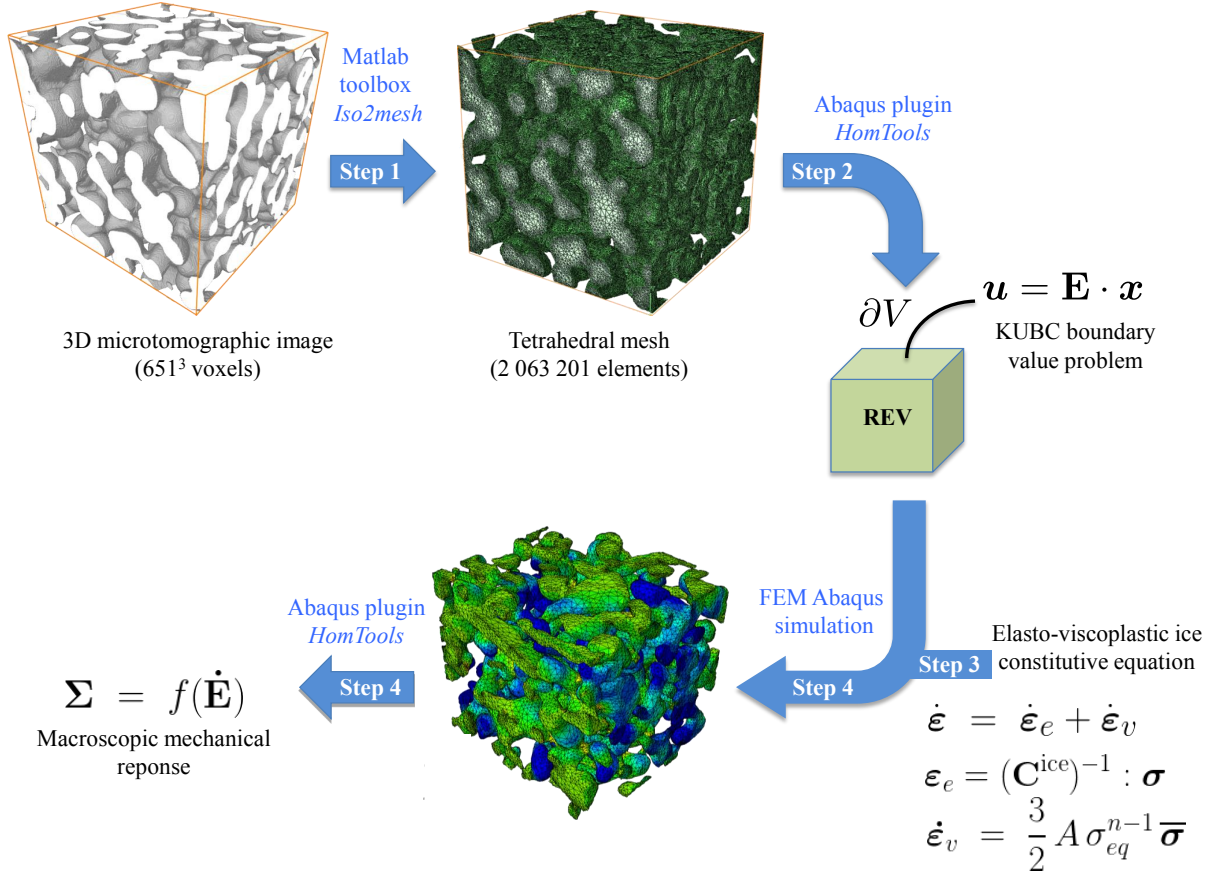
Figure 1. Four-step procedure used in order to transform 3-D microtomograph images of snow into finite element models and numerically solve KUBC homogenization boundary value problems.

Concerning the viscous part, at low strain rates, the non linear mechanical behavior of ice is usually described by a power law (Mellor, 1974; Schulson et al., 2009), i.e. the Norton Hoff in 3D (Lemaitre and Chaboche, 1985). Thus, we have

$$\dot{\boldsymbol{\varepsilon}}_v = \frac{3}{2} A \sigma_{\text{eq}}^{(n-1)} \overline{\boldsymbol{\sigma}}, \tag{2}$$

where A and n are two material parameters (which usually depend on the temperature), $\overline{\boldsymbol{\sigma}}$ is the deviatoric stress tensor and $\sigma_{\text{eq}}(\boldsymbol{\sigma})$ is the equivalent stress defined as

$$\sigma_{\text{eq}}(\boldsymbol{\sigma}) = \sqrt{\frac{3}{2} \overline{\boldsymbol{\sigma}} : \overline{\boldsymbol{\sigma}}} = \sqrt{\frac{3}{2} \bar{s}_2}, \qquad \overline{\boldsymbol{\sigma}} = \boldsymbol{\sigma} - \frac{1}{3} \text{Tr}(\boldsymbol{\sigma}) \mathbf{I}, \tag{3}$$

where $\mathbf{I}$ is the second order identity tensor, Tr is the trace operator and $\bar{s}_2$ is the second invariant of $\overline{\boldsymbol{\sigma}}$. It can be shown (Lemaitre and Chaboche, 1985) that the viscous strain rate tensor $\dot{\boldsymbol{\varepsilon}}_v$ derives from a viscous potential $\omega(\boldsymbol{\sigma})$ as

$$\dot{\boldsymbol{\varepsilon}}_v = \frac{\partial \omega}{\partial \boldsymbol{\sigma}} = \frac{d\omega}{d\sigma_{\text{eq}}} \frac{\partial \sigma_{\text{eq}}}{\partial \boldsymbol{\sigma}} = \frac{3}{2} \frac{d\omega}{d\sigma_{\text{eq}}} \frac{\overline{\boldsymbol{\sigma}}}{\sigma_{\text{eq}}}, \qquad \text{with} \quad \omega(\boldsymbol{\sigma}) = \frac{A}{n+1} \sigma_{\text{eq}}^{(n+1)}. \tag{4}$$

From (2) and (4), one can define the equivalent strain rate $\dot{\varepsilon}_{\mathrm{eq}}(\dot{\boldsymbol{\varepsilon}}_v)$ as the dual variable of the equivalent stress σ_{eq} such that

$$\dot{\varepsilon}_{\mathrm{eq}}(\dot{\boldsymbol{\varepsilon}}_v) = \sqrt{\frac{2}{3}\dot{\bar{\boldsymbol{\varepsilon}}}_v : \dot{\bar{\boldsymbol{\varepsilon}}}_v} = \sqrt{\frac{2}{3}}\bar{e}_2, \quad \text{with} \quad \dot{\varepsilon}_{\mathrm{eq}} = A\sigma_{\mathrm{eq}}^n, \tag{5}$$

where $\bar{e}_2$ is the second invariant of the deviatoric part of $\dot{\boldsymbol{\varepsilon}}_v$. If p_{v} stands for the volumetric mechanical dissipation, the equivalent stress and the equivalent strain rate verify

$$p_{\mathrm{v}} = \boldsymbol{\sigma} : \dot{\boldsymbol{\varepsilon}}_v = \bar{s}_2.\bar{e}_2 = \dot{\varepsilon}_{\mathrm{eq}}.\sigma_{\mathrm{eq}} = A\sigma_{\mathrm{eq}}^{(n+1)}. \tag{6}$$

At the microscopic scale, the viscoplastic deformation of ice is incompressible. Consequently the equivalent stress (resp. the equivalent strain rate) depends only on the second invariant $\bar{s}_2$ of $\overline{\boldsymbol{\sigma}}$ (resp. the second invariant $\bar{e}_2$ of $\dot{\bar{\boldsymbol{\varepsilon}}}_v$).

Overall, the ice matrix is thus modeled as an isotropic elasto-viscoplastic material in the finite element commercial software Abaqus. The values of the material constants used in this constitutive modeling, namely A, n, E and ν, are given in Table 1. It should be underlined that even if the most common values used for E and n are $E = 9$ GPa and $n = 3$, the ice Young's modulus values found in the literature range from 0.2 to 9.5 GPa (Chandel et al., 2014) and the values for n vary between 1.8 and 4.6 under usual loading (strain rate, stress) and temperature conditions (Scapozza and Bartelt, 2003; Schulson et al., 2009; Schleef et al., 2014). As a result, different values for E and n are considered in this study to give more insight on their influence on the homogenized viscoplastic behavior of snow.

Table 1. Mechanical parameters used in the elasto-viscoplastic modeling of ice implemented in Abaqus.

Parameters	Value
A	$1.5\ 10^{-3}\,\mathrm{MPa^{-n}.s^{-1}}$
n	2, 3, 4.5
E	325 MPa, 9 GPa
ν	0.3

2.2 Macro-strain paths definition (Step 4)

Given a time dependent macroscopic strain loading $\mathbf{E}(t)$, the KUBC homogenization problem to be solved reads as

$$
\begin{cases}
\operatorname{div}\boldsymbol{\sigma} & = & 0 & \text{for } \boldsymbol{x} \in V \\[2mm]
\boldsymbol{u} & = & \mathbf{E}(t)\cdot\boldsymbol{x} & \text{for } \boldsymbol{x} \in \partial V \\[2mm]
\boldsymbol{\varepsilon} & = & \dfrac{1}{2}\left(\boldsymbol{\nabla}\,\boldsymbol{u} + {}^{t}\boldsymbol{\nabla}\,\boldsymbol{u}\right) & \text{for } \boldsymbol{x} \in V \\[2mm]
\boldsymbol{\varepsilon} & = & \boldsymbol{\varepsilon}_e + \boldsymbol{\varepsilon}_v & \text{for } \boldsymbol{x} \in V \\[2mm]
\dot{\boldsymbol{\varepsilon}}_v & = & \dfrac{3}{2}A(\boldsymbol{x})\,\sigma_{\text{eq}}^{n-1}\,\boldsymbol{\sigma} & \text{for } \boldsymbol{x} \in V \\[2mm]
\boldsymbol{\sigma} & = & \dfrac{E(\boldsymbol{x})}{1+\nu}\left(\boldsymbol{\varepsilon}_e + \dfrac{\nu}{1-2\nu}\operatorname{Tr}(\boldsymbol{\varepsilon}_e)\mathbf{1}\right) & \text{for } \boldsymbol{x} \in V
\end{cases}
, \tag{7}
$$

where V stands for the domain occupied by the whole snow sample and ∂V its boundary. The spatial heterogeneity of the mechanical properties of snow is captured thanks to the functions $A(\boldsymbol{x})$ and $E(\boldsymbol{x})$ defined as

$$
A(\boldsymbol{x}) = \begin{cases} A & \text{if } \boldsymbol{x} \in V_i \\ 0 & \text{if } \boldsymbol{x} \in V\backslash V_i \end{cases} \quad \text{and} \quad E(\boldsymbol{x}) = \begin{cases} E & \text{if } \boldsymbol{x} \in V_i \\ 0 & \text{if } \boldsymbol{x} \in V\backslash V_i \end{cases}. \tag{8}
$$

where $V_i \subset V$ is the domain occupied by the ice matrix. Similarly to the elastic case (Wautier et al., 2015), the macroscopic stress tensor $\boldsymbol{\Sigma}$ is deduced from the knowledge of its microscopic counterpart thanks to the volume averaging

$$
\boldsymbol{\Sigma} = \frac{1}{|V|}\int_V \boldsymbol{\sigma}\,\mathrm{d}V = \langle\boldsymbol{\sigma}\rangle \tag{9}
$$

As a result, for a given macroscopic strain loading $\mathbf{E}(t)$, the macroscopic stress response $\boldsymbol{\Sigma}(t)$ is recovered. The implicit function linking these two second order tensors characterizes the homogeneous behavior of the snow sample considered and can be put in the form:

$$
\dot{\mathbf{E}} = \dot{\mathbf{E}}_e + \dot{\mathbf{E}}_v = \mathcal{F}(\boldsymbol{\Sigma}) \tag{10}
$$

where $\dot{\mathbf{E}}_e$ is the macroscopic elastic strain rate tensor and $\dot{\mathbf{E}}_v$ is the macroscopic viscous strain rate tensor. The elastic part can be expressed as, $\mathbf{E}_e = (\mathbf{C}^{\text{hom}})^{-1} : \boldsymbol{\Sigma}$, where $\mathbf{C}^{\text{hom}}$ is the homogenized stiffness tensor (Wautier et al., 2015). This tensor can be obtained by performing only six simulations on Representative Elementary Volumes extracted from 3D images. A single simulation is required if the snow microstructure is isotropic. By contrast, the homogenization of the visco-plastic behavior requires *a priori* an infinite number of numerical simulations. However, this number of simulations can be reduced by taking into account some theoretical results (Auriault et al., 1992; Suquet, 1993; Orgéas et al., 2007). Indeed, it can be shown that:

- The homogeneity of degree n of the microscopic viscous constitutive equation (2) is preserved in the homogenization process. In other words, the macroscopic viscous strain rate $\dot{\mathbf{E}}_v$ is a homogeneous function of degree n of the macroscopic

stress $\boldsymbol{\Sigma}$, and the macroscopic volumetric mechanical dissipation $\mathcal{P}_{\mathrm{v}} = \dot{\mathbf{E}}_v : \boldsymbol{\Sigma}$ is an homogeneous function of degree $n+1$ of $\boldsymbol{\Sigma}$

$$
\begin{cases}
\dot{\mathbf{E}}_v(\lambda\boldsymbol{\Sigma}) & = \quad \lambda^n\,\dot{\mathbf{E}}_v(\boldsymbol{\Sigma}) \\
\mathcal{P}_{\mathrm{v}}(\lambda\boldsymbol{\Sigma}) & = \quad \lambda\boldsymbol{\Sigma}:\dot{\mathbf{E}}_v(\lambda\boldsymbol{\Sigma}) \; = \; \lambda^{n+1}\,\mathcal{P}_{\mathrm{v}}(\boldsymbol{\Sigma})
\end{cases}
\quad , \qquad \forall\lambda\in\mathbb{R}.
\tag{11}
$$

As a result, the choice in the macroscopic strain rate $\dot{\mathbf{E}}_v$ can be reduced to the unit sphere in the second order tensor space, i.e. to strain rate tensors of norm $\sqrt{\dot{\mathbf{E}}_v : \dot{\mathbf{E}}_v} = 1$.

– The macroscopic dissipation potential $\Omega(\boldsymbol{\Sigma})$ is the volume-average of the local dissipation potential ω

$$
\Omega(\boldsymbol{\Sigma}) \; = \; \frac{1}{|V|}\int_V \omega(\boldsymbol{\sigma})\,\mathrm{d}V = \langle\omega(\boldsymbol{\sigma})\rangle
\tag{12}
$$

and consequently, as at the microscopic scale (see equation (4)), we have

$$
\dot{\mathbf{E}}_v = \frac{\partial\Omega}{\partial\boldsymbol{\Sigma}} = \frac{\mathrm{d}\Omega}{\mathrm{d}\Sigma_{\mathrm{eq}}}\frac{\partial\Sigma_{\mathrm{eq}}}{\partial\boldsymbol{\Sigma}}, \qquad \text{with} \quad \Omega(\boldsymbol{\Sigma}) = \frac{A}{n+1}\Sigma_{\mathrm{eq}}^{n+1}
\tag{13}
$$

where $\Sigma_{\mathrm{eq}}(\boldsymbol{\Sigma})$ is the macroscopic equivalent stress.

$\Sigma_{\mathrm{eq}}(\boldsymbol{\Sigma})$ verifies

$$
\mathcal{P}_{\mathrm{v}} = \boldsymbol{\Sigma} : \dot{\mathbf{E}}_v = \dot{\mathrm{E}}_{\mathrm{eq}}.\Sigma_{\mathrm{eq}} = A\Sigma_{\mathrm{eq}}^{n+1}
\tag{14}
$$

with $\dot{\mathrm{E}}_{\mathrm{eq}}(\dot{\mathbf{E}}_v)$ the macroscopic equivalent strain rate defined by duality.

As a result, the macroscopic viscoplastic law (13) is perfectly defined if the macroscopic equivalent stress Σ_{eq} is known. The latter equation (14) shows that this macroscopic equivalent stress Σ_{eq} can be fitted on iso-mechanical dissipation surfaces in the space associated with $\boldsymbol{\Sigma}$. Let us remark that the shape and size of such iso-mechanical dissipation surfaces results from the strong coupling between the microstructure and the non-linear behavior of the ice under consideration. The relation (14) also shows the equivalent stress can be obtained whatever the chosen A value. In the case of general anisotropy, the form of Σ_{eq} can be formulated within the framework defined by the theory of representation of anisotropic tensor functions (Smith, 1971; ?). It is also important to mention that for the ice matrix, the overall response of snow is insensitive to the sign of $\boldsymbol{\Sigma}$ as a consequence of definition (4). This condition may be expressed as $\Omega(\boldsymbol{\Sigma}) = \Omega(-\boldsymbol{\Sigma})$. Finally, let us remark that by definition (see (13) and (14)), the macroscopic strain rate $\dot{\mathbf{E}}_v$ is normal to iso-mechanical dissipation surfaces (normality rule).

In the following, for the sake of simplicity, we will suppose that the macroscopic viscoplastic behavior of snow is isotropic. In this particular case, for a given value of n, it can be shown (Abouaf, 1985; Geindreau et al., 1999b; Danas et al., 2008) that the macroscopic equivalent stress is written:

$$
\Sigma_{\mathrm{eq}}(\boldsymbol{\Sigma}) = \Sigma_{\mathrm{eq}}(S_1, \bar{S}_2, \bar{S}_3, \phi)
\tag{15}
$$

where ϕ is the snow porosity and $(S_1, \bar{S}_2, \bar{S}_3)$ are the three invariants of the macroscopic stress tensor $\mathbf{\Sigma}$ defined as:

$$S_1 = \text{Tr}(\mathbf{\Sigma}), \quad \bar{S}_2 = \sqrt{\overline{\mathbf{\Sigma}} : \overline{\mathbf{\Sigma}}}, \quad \bar{S}_3 = \det(\overline{\mathbf{\Sigma}}), \quad \text{with} \quad \overline{\mathbf{\Sigma}} = \mathbf{\Sigma} - \frac{S_1}{3}\mathbf{I}. \tag{16}$$

Similarly, the macroscopic equivalent strain rate $\dot{\text{E}}_{\text{eq}}$ takes the form

$$\dot{\text{E}}_{\text{eq}}(\dot{\mathbf{E}}_v) = \dot{\text{E}}_{\text{eq}}(E_1, \bar{E}_2, \bar{E}_3, \phi) \tag{17}$$

where $(E_1, \bar{E}_2, \bar{E}_3)$ are the invariants of the strain rate tensor $\dot{\mathbf{E}}_v$ defined as

$$E_1 = \text{Tr}(\dot{\mathbf{E}}_v), \quad \bar{E}_2 = \sqrt{\dot{\overline{\mathbf{E}}}_v : \dot{\overline{\mathbf{E}}}_v}, \quad \bar{E}_3 = \det(\dot{\overline{\mathbf{E}}}_v), \quad \text{with} \quad \dot{\overline{\mathbf{E}}}_v = \dot{\mathbf{E}}_v - \frac{E_1}{3}\mathbf{I}. \tag{18}$$

In contrast with the microscopic scale (see equation (3)), the macroscopic equivalent stress (15) depends on the three invariants $(S_1, \bar{S}_2, \bar{S}_3)$ of the macroscopic stress tensor $\mathbf{\Sigma}$. Indeed, at the macroscopic scale, the viscoplastic snow deformation is compressible. This compressibility, characterized by E_1, depends on the level of the mean pressure $(S_1/3)$ applied on the snow sample, as well as the mean shear stress $(\bar{S}_2)$. The third invariant $\bar{S}_3$ characterizes the loading type and is linked to the Lode angle θ in the stress space (Lemaitre and Chaboche, 1985; Danas et al., 2008)

$$\cos(3\theta) = \frac{27}{2}\frac{\bar{S}_3}{\Sigma_{\text{eq}}^3}. \tag{19}$$

As a first approximation, it seems reasonable to assume that the influence of the third invariant $\bar{S}_3$ is negligible (Green, 1972; Abouaf, 1985; Geindreau et al., 1999b; Fritzen et al., 2012). Consequently, the macroscopic volumetric mechanical dissipation $\mathcal{P}_{\text{v}}$ depends on the first and second stress and strain invariants and not only on the second ones as at the microscale (6).

$$\mathcal{P}_{\text{v}} = \mathbf{\Sigma} : \dot{\mathbf{E}}_v = \text{E}_{\text{eq}}.\Sigma_{\text{eq}} = A\Sigma_{\text{eq}}^{n+1} = \frac{1}{3}E_1.S_1 + \bar{E}_2.\bar{S}_2. \tag{20}$$

The relation (20) shows that, for a given snow porosity, the equivalent macroscopic stress Σ_{eq} can be fitted on iso-volumetric mechanical dissipation curves in the plane $(S_1/3, \bar{S}_2)$. These isodissipation curves can be obtained by plotting the values $(S_1/3, \bar{S}_2)$ corresponding to different loading conditions defined by $(E_1, \bar{E}_2)$. Therefore, the choice was made to run numerical simulation for seven diagonal strain rate tensors defined such that the loading direction in the plane $(E_1, \bar{E}_2)$ varies from $0°$ to $90°$. More explicitly, $\dot{\mathbf{E}}$ applied on the sample is taken as

$$\dot{\mathbf{E}} = \dot{\text{E}}_{\text{ref}}\begin{pmatrix} 1 & 0 & 0 \\ 0 & \eta & 0 \\ 0 & 0 & \eta \end{pmatrix}, \tag{21}$$

with $\dot{\text{E}}_{\text{ref}} = 10^{-7}\text{ s}^{-1}$ and $\eta \le 1$ such that $\dfrac{\bar{E}_2}{E_1} = \sqrt{\dfrac{2}{3}}\dfrac{1-\eta}{1+2\eta} = \tan\theta, \quad \theta \in \{0°, 9°, 18°, 30°, 45°, 65°, 90°\}.$

Finally, to be consistent with the isotropy hypothesis, numerical simulations have been performed on the most isotropic snow samples with respect to their elastic behavior from the snow database used in Wautier et al. (2015). With reference to the

supporting information of the cited paper (Wautier et al., 2015), the name and the principal characteristics of each sample are recalled in Table 2. The porosities of the selected samples vary from 0.43 to 0.87, which covers almost the entire range of porosity of seasonal snow. Each sample presents similar correlation lengths (ℓ_1, ℓ_2, ℓ_3) (Löwe et al., 2013; Calonne et al., 2014) in the three space directions. All the simulations have been performed on volumes extracted from the 3D images sufficiently large to be considered as REV, as in Wautier et al. (2015).

Table 2. Names and principal characteristics of the six snow images of Wautier et al. (2015) used in this study.

Sample name	Snow type	Dim (px)	Dim (mm)	Resolution (μm/px)	Snow density (kg/m^3)	Porosity	Correlation lengths (ℓ_1, ℓ_2, ℓ_3) (μm)
PP_123kg_600	PP	600	2.95	4.91	123.31	0.87	(64, 64, 65)
RG_172kg_600	RG	600	2.95	4.91	172.74	0.81	(92, 94, 97)
RG_256kg_512	RG	512	2.51	4.91	256.28	0.72	(113, 111, 110)
RG_1600	RG	600	4.46	7.43	330.13	0.64	(117, 111, 108)
RG_430kg_651	RG	651	5.61	8.61	430.59	0.53	(83, 82, 81)
MF_522kg_542	MF	542	5.42	10.00	522.31	0.43	(138, 134, 133)

3 Post-processing procedure: from macroscopic stress response to a homogenized model for snow visco-plasticity

From the homogenization procedure presented in the previous section, the time response of a given isotropic snow sample is recovered for the seven loading directions in the plane of the strain invariants $(E_1, \bar{E}_2)$ given by the equation (21). The strain rate is applied on each sample during less than 40,000 s, corresponding to a volumetric strain smaller than 1.2 %. The overall viscous behavior of the snow samples is deduced thanks to a post-processing procedure consisting in the three steps described in this section (steps a to c) and summarized in Figure 2.

3.1 Extracting the viscous response (step a)

Because snow is locally modeled as an elasto-visco-plastic material in Abaqus (see subsection 2.1), the macroscopic time response $\boldsymbol{\Sigma}(t) = \frac{1}{|V|} \int_V \boldsymbol{\sigma}(\boldsymbol{x}) \, \mathrm{d}V$ deduced from numerical simulations does not result only from the viscous behavior. In the case where the ice viscosity is activated everywhere in the ice skeleton, the macroscopic stress $\boldsymbol{\Sigma}(t)$ corresponding to a constant strain rate should stabilize around a constant value according to equation (2). However, due to the complex ice skeleton geometry, the ice viscosity is not uniformly activated and the time response of $\boldsymbol{\Sigma}(t)$ is influenced by the ice elastic behavior even in the long term. Based on the material parameters A, n, and E, and the typical imposed strain rate $\dot{\mathrm{E}}_{\mathrm{ref}}$, a characteristic time τ can be introduced as the ratio between the ice viscosity $\eta(\dot{\mathrm{E}}_{\mathrm{ref}}) = (\dot{\mathrm{E}}_{\mathrm{ref}}/A)^{1/n}/\dot{\mathrm{E}}_{\mathrm{ref}}$ and the Young modulus E

$$\tau = \frac{\eta(\dot{\mathrm{E}}_{\mathrm{ref}})}{E} = \frac{1}{E} \left(A^{-\frac{1}{n}} \, \dot{\mathrm{E}}_{\mathrm{ref}}^{\frac{1-n}{n}} \right). \tag{22}$$

Step a: - Compute the mechanical response $(S_1(t), \bar{S}_2(t))$ for a given constant strain rate $\dot{\mathbf{E}}$

- Determine the viscous response $(S_1^v, \bar{S}_2^v)$ associated with the strain state $(E_1, \bar{E}_2)$

Step b: - For each loading given in Eq. (21), compute the associated viscous dissipated power with Eq. (22)

- Rescale the numerical points on an isodissipation curve thanks to Eq. (23)

Step c: - Fit an Abouaf's model thanks to Eq. (24) and (27)

Figure 2. Three-step post-processing procedure used in order to formulate a homogenized viscous constitutive equation.

The typical stress response of a snow sample under a constant given strain rate versus the dimensionless time (t/τ) is illustrated in Figure 3 for the snow sample *RG_1600* (Table 2) for different values of n and E. In all the cases, the mechanical response is characterized by a transient regime driven by the elastic properties followed by a permanent regime dominated by the viscoplastic behavior. As illustrated by the comparison between the cases $(n, E) = (4.5, 325 \text{ MPa})$ and $(n, E) = (4.5, 9 \text{ GPa})$, the responses $S_1(t/\tau)$ and $\bar{S}_2(t/\tau)$ are independent of the Young's modulus value chosen. On the contrary, the mechanical response is influenced by the n value.

As a result, for a given value of n and whatever the Young's modulus value, the viscoplastic behavior of snow can be characterized by computing the intersection point between the initial and final asymptotes of the curves $S_1(t/\tau)$ and $\bar{S}_2(t/\tau)$ in Figure 3. The obtained values for the two stress invariants are noted S_1^v and $\bar{S}_2^v$ and are systematically used in the rest of this paper as the snow viscous homogeneous response to a given imposed constant macroscopic strain rate. The top graph in Figure 2 illustrates this step of the post-processing procedure.
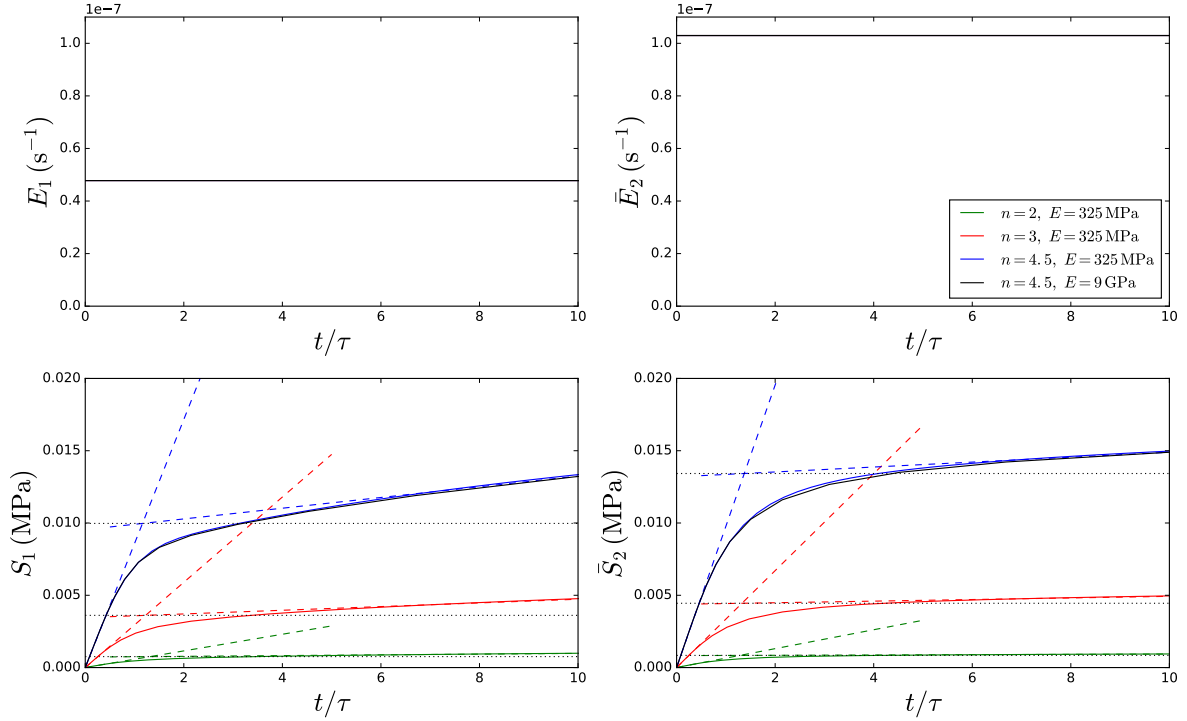
Figure 3. Imposed strain rate (top) and stress response (bottom) versus dimensionless time (t/τ) for the sample *RG_1600* (see Table 2). The loading strain rate is characterized by $\theta = 65°$ in equation (21). Two Young's moduli and three values of n are considered.

3.2 Computing isodissipation curves (step b)

For a given snow sample of porosity ϕ and for each applied loading path (21), the macroscopic volumetric mechanical dissipation $\mathcal{P}_\mathrm{v}$ (20) is computed as

$$\mathcal{P}_\mathrm{v} = \frac{1}{3} E_1 . S_1^v + \bar{E}_2 . \bar{S}_2^v, \tag{23}$$

where S_1^v and $\bar{S}_2^v$ are the characteristic stress invariants obtained in the first step of the post-processing process (Figure 2). Each loading path leads to different values of $\mathcal{P}_\mathrm{v}$. However, iso-mechanical dissipation points in the plane $(S_1/3, \bar{S}_2)$ can be recovered thanks to the homogeneity property (11). Given an arbitrary value of $\mathcal{P}_\mathrm{v}^\circ = 1\,\mathrm{Pa.s}^{-1}$, the corresponding macroscopic strain and stress invariants are computed as

$$(E_1^\circ, \bar{E}_2^\circ) = \left(\frac{\mathcal{P}_\mathrm{v}^\circ}{\mathcal{P}_\mathrm{v}}\right)^{n/(n+1)} (E_1, \bar{E}_2), \quad \text{and} \quad (S_1^\circ, \bar{S}_2^\circ) = \left(\frac{\mathcal{P}_\mathrm{v}^\circ}{\mathcal{P}_\mathrm{v}}\right)^{1/(n+1)} (S_1^v, \bar{S}_2^v). \tag{24}$$

12

Thanks to this rescaling, the seven homogenization tests (21) enable the description of an isodissipation curve in the plane of the stress invariants $(S_1/3, \bar{S}_2)$ as illustrated in Figure 2 (step b). For each point $(S_1^\circ/3, \bar{S}_2^\circ)$ on this graph, the associated flow vector $(E_1^\circ, \bar{E}_2^\circ)$ is plotted. The viscous dissipated power is thus simply equivalent to the scalar product $(S_1^\circ/3, \bar{S}_2^\circ) \cdot (E_1^\circ, \bar{E}_2^\circ)$.

3.3 Abouaf's model (step c)

Within the framework presented in section 2.2, Abouaf (1985) has suggested to use the macroscopic equivalent stress initially proposed by Green (1972) to describe the viscoplastic behavior of metal powders at high temperatures. This macroscopic equivalent stress $\Sigma_{\text{eq}}(\boldsymbol{\Sigma})$, is written

$$\Sigma_{\text{eq}}(\boldsymbol{\Sigma}) = \Sigma_{\text{eq}}(S_1, \bar{S}_2, \phi) = \sqrt{f(\phi) S_1^2 + \frac{3}{2} c(\phi) \bar{S}_2^2}, \tag{25}$$

where $f(\phi)$ and $c(\phi)$ are two material functions which depend on snow porosity only for a given power law creep exponent n. When $\phi = 0$, we have $f(\phi) = 0$ and $c(\phi) = 1$ in order to recover the equivalent viscous stress of the ice matrix (3): $\Sigma_{\text{eq}}(\boldsymbol{\Sigma}, \phi = 0) = \sigma_{\text{eq}}(\boldsymbol{\sigma})$. From the definition of the viscous strain in (13) together with the previous definition of the equivalent stress in (25), it can be shown that

$$\dot{\mathbf{E}}_v = A \Sigma_{\text{eq}}^{n-1} \left(f(\phi) S_1 \mathbf{I} + \frac{3}{2} c(\phi) \overline{\boldsymbol{\Sigma}} \right). \tag{26}$$

As a result, the corresponding macroscopic equivalent strain rate introduced in equation (20) reads

$$\dot{\mathrm{E}}_{\text{eq}}(\dot{\mathbf{E}}_v) = \dot{\mathrm{E}}_{\text{eq}}(E_1, \bar{E}_2, \phi) = \sqrt{\frac{E_1^2}{9 f(\phi)} + \frac{2}{3} \frac{\bar{E}_2^2}{c(\phi)}}. \tag{27}$$

For a given porosity ϕ, the combination of (25) and (20) provides an implicit definition of $f(\phi)$ and $c(\phi)$ such that, for all $(S_1, \bar{S}_2)$

$$\Sigma_{\text{eq}}(S_1, \bar{S}_2, \phi) = \sqrt{f(\phi) S_1^2 + \frac{3}{2} c(\phi) \bar{S}_2^2} = \left(\frac{\mathcal{P}_v^\circ}{A} \right)^{1/(n+1)}. \tag{28}$$

In the present work, the optimal values for $f(\phi)$ and $c(\phi)$, where $0.43 < \phi < 0.87$, were obtained by minimizing the quadratic error between the model and the numerical points.

4 Results and discussion

The homogenization and the post-processing procedure presented in the previous sections are applied to six isotropic snow samples of various densities chosen in the same database as Wautier et al. (2015) and already introduced in Table 2. In Figure 4, the seven points $(S_1^\circ/3, \bar{S}_2^\circ)$ corresponding to the strain rates of equation (21) are represented for these six snow samples in the plane of the two first stress invariants for $n = 4.5$. Similar results have been obtained for the other values of n, as shown on the Figure 5. The corresponding strain flow vectors $(E_1^\circ, \bar{E}_2^\circ)$ are shown by solid arrows and the isodissipation curves corresponding to the fitted Abouaf model are represented by solid lines. The optimal values for f and c obtained for each snow type are presented on Figure 4 and reported in Table 3 for $n \in \{2, 3, 4.5\}$. It should be underlined here that each isodissipation curve is typical of a given snow characterized by its density and thus each curve is also an iso-density curve.
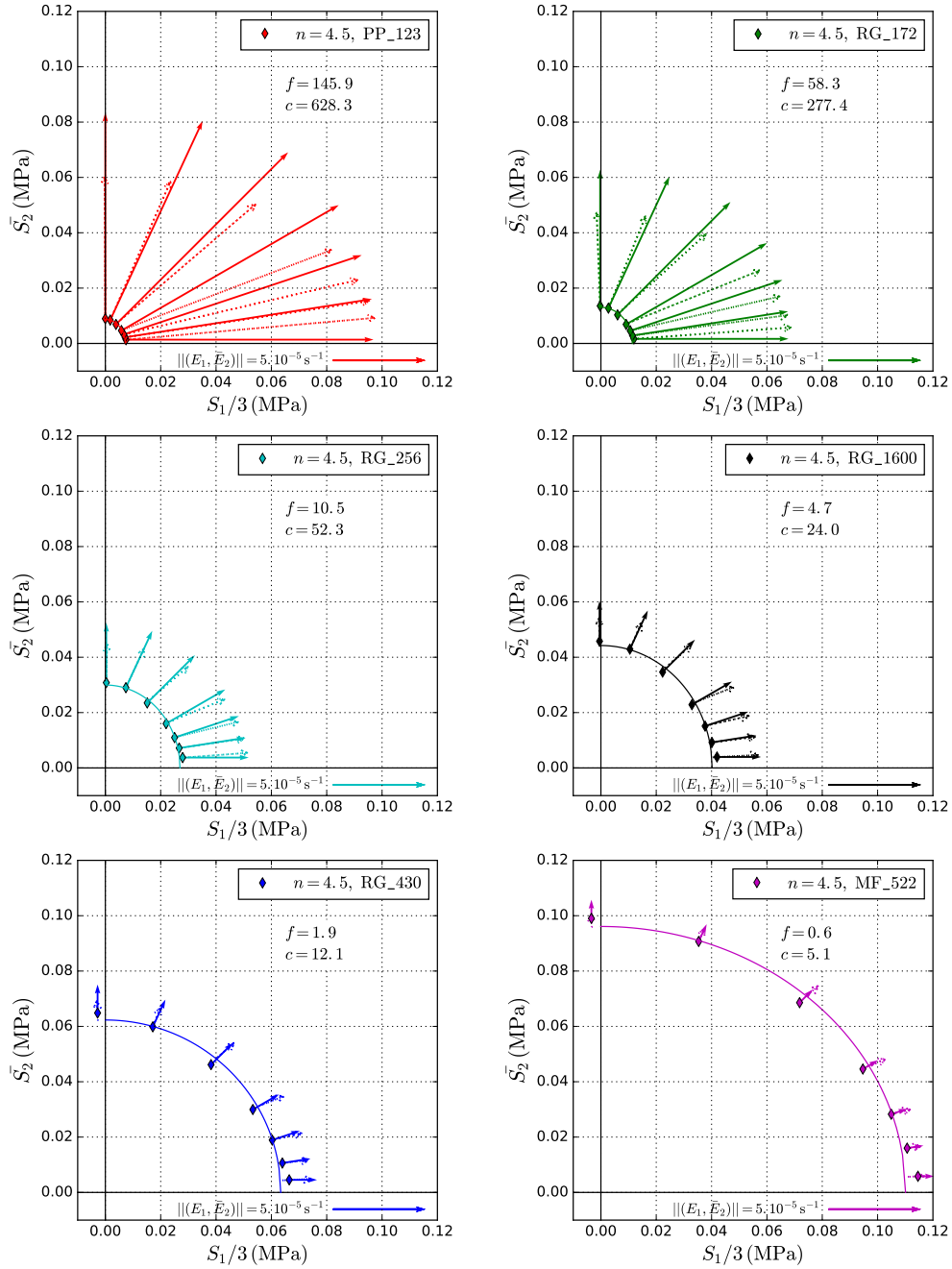
Figure 4. Isodissipation curves in the plane of the stress invariants $(S_1, \bar{S}_2)$ corresponding to $n = 4.5$ and to an arbitrary dissipated power $\mathcal{P}_v^\circ$ for the six snow samples of Table 2 in increasing density order. The associated strain flow vectors $(E_1^\circ, \bar{E}_2^\circ)$ are represented by solid arrows. Abouaf models are fitted to the numerical points (solid lines) and theoretical values of strain flow vectors are shown (dashed arrows). Parameters f and c of the fits are shown on the graphs and summarized in Table 3.

4.1 Isodissipation curves for various snow samples

The comparison between the simulated points and the Abouaf's model shows overall good agreement in terms of stress prediction even if a systematic slight deviation is observed between the model and the simulated points for the highest S_1 values. It should also be noticed that the stress state corresponding to an isotropic strain rate ($\bar{E}_2 = 0$) is not completely isotropic ($\bar{S}_2 \neq 0$). This feature cannot be captured by the Abouaf modeling, which assumes a perfect isotropic behavior of the material. Even if the snow samples used in this study were selected as isotropic as possible, a slight anisotropy should account for the observed residual deviatoric stress component existing under an isotropic strain loading.

As already mentioned in section 2.2, the viscous behavior of snow should be insensitive to the sign of Σ as the ice matrix behave exactly the same in tension and in compression. In the stress space $(S_1/3, \bar{S}_2)$, this results in the symmetry of the isodissipation curves with respect to the axis $S_1/3 = 0$. Provided that the isodissipation curves are smooth, their tangent for $S_1/3 = 0$ is horizontal, which is respected in Figure 4. It must be mentioned that when snow is subjected to large strain levels, geometrical effects will introduce non linear effects and the mechanical response in tension will differ from the one in compression. These effects can also be investigated using the same homogenization procedure.

The overall viscoplastic response of snow is of course sensitive to the n exponent of the Norton Hoff's law (2) used for the ice (see section 3.1). As for example, in Figure 5, the influence of n onto the isodissipation curves is shown for the snow sample *MF_522*. Similar results have been obtained on the other samples. As expected, for a given value $\mathcal{P}_v^\circ$, the size of the isodissipation curves increases with n (since the ice viscosity $\eta(\dot{\mathrm{E}}_{\mathrm{ref}})$ increases) but their shape remains unchanged. They can be deduced from each other by simple dilation.

4.2 Density dependence of the isodissipation curves

As snow density increases, the isodissipation curves tend to expand, and conversely the flow vectors tend to get smaller. In terms of physics, this means that the denser snow is, the smaller the applied strain rate in order to dissipate the same level of

Table 3. Optimal values for the parameters f and c of the Abouaf's equivalent stress (25) for three n values.

Sample name	Porosity	$n=2$ f	c	$n=3$ f	c	$n=4.5$ f	c
PP_123kg_600	0.87	36.0	150	79.7	336	146	628
RG_172kg_600	0.81	16.3	75.7	33.5	156	58.3	277.4
RG_256kg_512	0.72	4.05	20.5	6.98	34.7	10.5	52.3
RG_1600	0.64	2.07	11.0	3.32	17.0	4.70	24.0
RG_430kg_651	0.53	0.915	6.38	1.40	9.12	1.89	12.1
MF_522kg_542	0.43	0.354	3.32	0.503	4.26	0.630	5.07
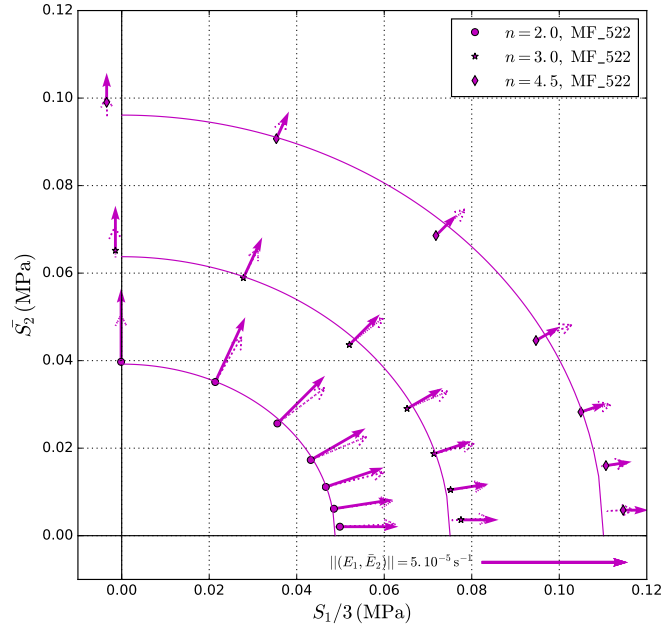
Figure 5. Influence of the exponent n onto the isodissipation curves ($\mathcal{P}_\mathrm{v} = \mathcal{P}_\mathrm{v}^\circ$) for the particular snow sample *MF_522*. The associated strain flow vectors $(E_1^\circ, \bar{E}_2^\circ)$ are represented by solid arrows. Abouaf models are fitted to the numerical points (solid lines) and theoretical values of strain flow vectors are shown (dashed arrows).

viscous power. In the meantime the applied stress should be increased. This is consistent with the fact that fresh snow tends to get denser more rapidly than already compacted snow under the same imposed loading.

The density dependence of snow viscous behavior is fully described by the evolution of $f(\phi)$ and $c(\phi)$ with respect to snow compacity ($\rho_\mathrm{snow}/\rho_\mathrm{ice} = 1-\phi$) represented in Figure 6 for $n \in \{2, 3, 4.5\}$. As snow density increases in Figure 6, the parameter

5   values decrease, which is consistent with the implicit definition of the isodissipation curves in equation (25). For a given equivalent stress Σ_eq, higher values for f and c will result in lower stress invariants S_1 and $\bar{S}_2$ as observed in Figure 4. Concerning the influence of n, the observed increase in f and c is consistent with the dilation of the isodissipation curves observed in Figure 5.

Different expressions of the material functions $f(\phi)$ and $c(\phi)$ have been proposed in the past based on experimental data on

10   metal powders (Abouaf, 1985; Abouaf and Chenot, 1988; Geindreau et al., 1999b), micromechanical modeling (cell model - Duva and Crow (1992)) or numerical simulations on simple microstructures (Sofronis and McMeecking, 1992). These functions have been identified in a restricted range of porosity (dense materials with $\phi < 0.4$). We propose to fit our numerical results using the expressions proposed by Geindreau et al. (1999b). In order to account for the change in the porosity range between metal powders and snow, the compacity limit value of 0.57 is set equal to zero. As a result, the proposed functions are
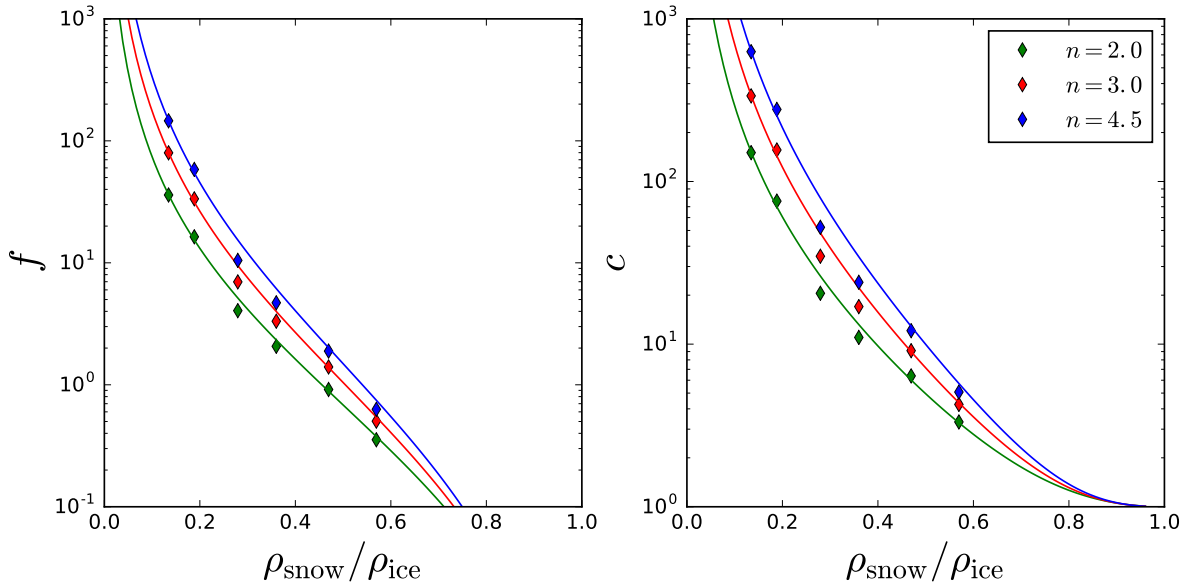
Figure 6. Evolution of the Abouaf coefficients f and c (numerical results as diamond points, functions (29) as solid lines) with respect to snow compacity for different n values.

written

$$
\begin{cases}
f(\phi) = a \left(\dfrac{\phi}{1-\phi} \right)^p \\
c(\phi) = 1 + b \left(\dfrac{\phi}{1-\phi} \right)^q
\end{cases}
, \quad (a,b,p,q) \in \mathbb{R}^4.
\tag{29}
$$

The above fits respect the theoretical values $f(0) = 0$ and $c(0) = 1$ already mentioned in section 3.3. For a highly porous snow ($\phi \to 1$), an infinitely small stress level would be needed in order to produce a high viscous dissipation. This is consistent

5   with the infinitely high values for f and c proposed by the above functions (29). These functions allow a good description of the numerical points resulting from the homogenization of the six snow samples (Table 3) and are represented by solid lines in Figure 6 for $n \in \{2, 3, 4.5\}$. As a result, they may stand for a general formulation for the viscous isotropic behavior of snow according to its porosity through the four n-dependent parameters (a, b, p, q) given in Table 4. For the sake of illustration, the evolution of the coefficients a, p, b and q with respect to n is shown in Figure 7. Let us remark that the parameters a and b

10   are close to the ones obtained for metal powders by Geindreau et al. (1999b). However, the exponents corresponding to the snow case are approximately twice bigger, which is linked to a more pronounced dependence on the porosity for very porous materials.

Another interesting feature which can be highlighted in Figure 4 is the fact that the isodissipation curves are closed for all the snow samples under consideration. This contrasts with the shape of ice isodissipation curves in the plane $(S_1/3, \bar{S}_2)$ which are

17

Table 4. Optimal parameters chosen for the expressions (29) for different n values.

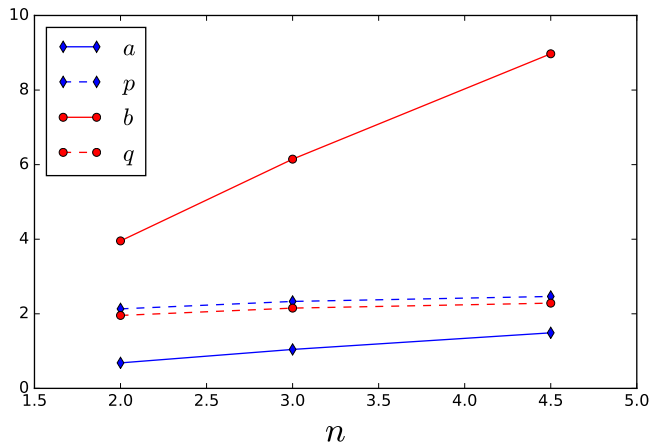|	$n = 2$	$n = 3$	$n = 4.5$
a	0.68	1.0	1.5
p	2.1	2.3	2.5
b	4.0	6.1	8.9
q	2.0	2.2	2.3

Figure 7. Evolution of the fitted coefficients a, p, b and q with respect to the exponent n of the ice Norton Hoff constitutive behavior.

represented by horizontal straight lines. Indeed, the corresponding viscous power doesn't depend on S_1 since the constitutive equation (2) for ice only involves the deviatoric stress $\bar{\sigma}$. The ability of snow to dissipate significant energy even under an isotropic loading ($\bar{S}_2 = 0$) is due to its porosity. Indeed, even under this type of macroscopic loading conditions, some regions of the snow microstructure experience a non zero deviatoric loading, which activates locally the viscous behavior of ice. Even if this deviatoric loading vanishes on average, the mean viscous dissipated power only piles up, which results in closed isodissipation curves. Their shapes provide information about the ability of an isotropic macroscopic loading to locally activate the ice viscous behavior. Based on the Abouaf formulation (25), the ratio between the maximum isotropic stress $S_1^{\mathrm{max}}/3$ and the maximum deviatoric stress $\bar{S}_2^{\,\mathrm{max}}$ can be expressed for each sample as

$$\frac{(S_1^{\mathrm{max}}/3)}{\bar{S}_2^{\,\mathrm{max}}} = \sqrt{\frac{c}{6f}}. \tag{30}$$

As snow is always submitted to a mechanical loading which can be decomposed into a deviatoric part and an isotropic part, this ratio provides a measure of the relative contribution of the isotopic part of the mechanical loading in the activation of the ice viscosity. The bigger this ratio, the smaller the activation degree. The evolution of this ratio is plotted in Figure 8 as a function of snow compacity for $n \in \{2, 3, 4.5\}$. The diamond points are computed using the values for f and c presented in Table 3 and the solid line is computed using the two functions (29) with the parameters presented in Table 4. The increase in this ratio with
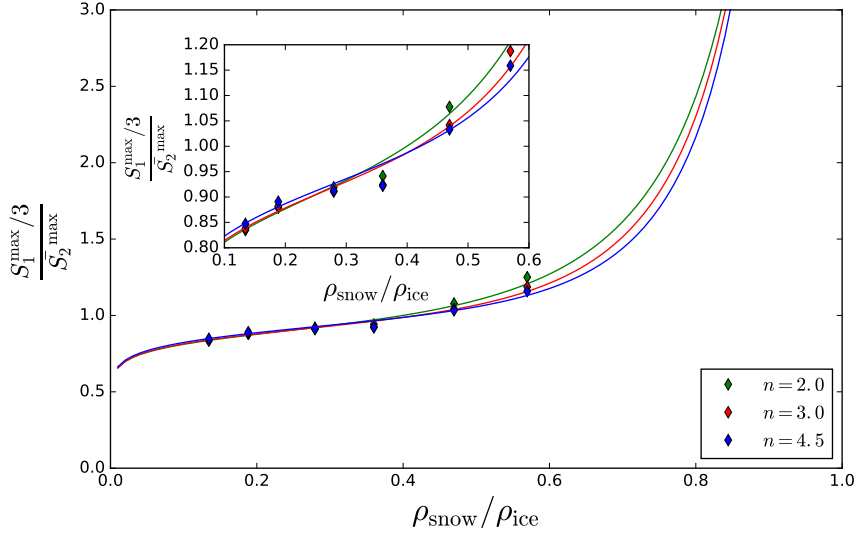
Figure 8. Aspect ratios $(S_1^{\max}/3)/S_2^{\max}$ of the Abouaf models with respect to snow compacity. Numerical results are represented with diamond points, results computed using functions (29) with solid lines.

snow density highlights the fact that deviatoric fluctuations get smaller under isotropic loading conditions as snow gets denser. In other words, the ice viscosity is more difficult to activate for dense snow than for fresh snow. The divergence of the solid line around 1 corresponds to the limit case of ice where $S_1^{\max}$ becomes infinite as predicted by (3). On this Figure, the dependence on the n value is very limited which highlights the fact that n doesn't have any influence on the shape of the isodissipation curves but only on the stress level leading to a given isodissipation as already seen in Figure 5.

4.3 Normality rule

The proposed macroscopic modeling is formulated within the framework of associated viscoplasticity. In other words, the flow direction $\dot{\mathbf{E}}$ is by construction supposed to be orthogonal to the isodissipation curves (see equation (13)). In the space composed of the two first stress and strain invariants' planes, for an isodissipation curve corresponding to Σ_{eq}, this normality is written

$$
\begin{pmatrix} E_1 \\ \bar{E}_2 \end{pmatrix} \propto \begin{pmatrix} \dfrac{3\partial\Sigma_{\mathrm{eq}}}{\partial S_1} \\ \dfrac{\partial\Sigma_{\mathrm{eq}}}{\partial \bar{S}_2} \end{pmatrix}. \tag{31}
$$

In the case of the Abouaf's model (see equation (25)), the theoretical values of the strain flow vectors associated to the seven points in Figure 4 is written

$$
\begin{pmatrix} E_1 \\ \bar{E}_2 \end{pmatrix} = A\,\Sigma_{\mathrm{eq}}^{n-1} \begin{pmatrix} 3f(\phi)\,S_1 \\ \frac{3}{2}c(\phi)\,\bar{S}_2 \end{pmatrix}. \tag{32}
$$

19

In Figures 4 and 5, the theoretical values of the strain flow vectors are represented by dashed arrows for the radial projections of the numerical points on the Abouaf fits. The overall comparison with their numerical counterparts represented by solid arrows is quite satisfactory, especially for the densest snows. However, concerning the flow direction, the Abouaf's model tends to over-predict the strain deviatoric component for high deviatoric stresses $\bar{S}_2$ and to under-predict the strain deviatoric component for low deviatoric stresses except for the direction $\theta = 0°$. In terms of magnitude, the Abouaf's model tends to under-predict the intensity of the flow for deviatoric loading.

The observed difference between theoretical and numerical flow vectors actually results from the slight misfit between the Abouaf models and the numerical points, which is amplified by the radial projection procedure used in order to compute the theoretical flow vectors. Moreover, the validity of normality rule tends to get less accurate as the porosity of the material increases. A similar trend has been already observed in the case of power law fluid flow through porous media (Orgéas et al., 2007). Overall, the Abouaf's model presented in section 3.3 provides a satisfactory modeling of snow viscous behavior on the whole range of investigated densities.

5   Application to classical laboratory tests

In the case of isotropic snow microstructures, the homogenized constitutive viscous behavior developed in this paper can be summarized as follow:

$$\dot{\mathbf{E}}_v \; = \; \dot{\mathrm{E}}_{\text{eq}} \frac{\partial \Sigma_{\text{eq}}}{\partial \boldsymbol{\Sigma}} \; = \; A\Sigma_{\text{eq}}^{n-1} \left(f(\phi)S_1\mathbf{I} + \frac{3}{2}c(\phi)\overline{\boldsymbol{\Sigma}} \right) \tag{33}$$

with

$$\Sigma_{\text{eq}}(S_1,\bar{S}_2,\phi) \; = \; \sqrt{f(\phi)\,S_1^2 + \frac{3}{2}c(\phi)\,\bar{S}_2^2}, \qquad \dot{\mathrm{E}}_{\text{eq}}(E_1,\bar{E}_2,\phi) = \sqrt{\frac{E_1^2}{9f(\phi)} + \frac{2}{3}\frac{\bar{E}_2^2}{c(\phi)}}, \tag{34}$$

and

$$f(\phi) \; = \; a\left(\frac{\phi}{1-\phi}\right)^p, \qquad c(\phi) \; = \; 1 + b\left(\frac{\phi}{1-\phi}\right)^q \tag{35}$$

where n and A account for the ice viscosity (Table 1) and a, p, b and q account for snow porosity (Table 4).

In the following, the mechanical responses of the proposed model are analyzed and compared in the case of classical laboratory tests (Figure 9). In this Figure, the situation (a) corresponds to the oedometric compression test in which the radial deformation E_{rr} of the snow sample is prevented. Snow mechanical response is then characterized by the relationship between the axial stress Σ_{zz} and the axial strain rate $\dot{E}_{zz}$. The situation (b) corresponds to the general triaxial compression test in which the radial stress Σ_{rr} is prescribed and kept constant. From this general setting, two particular cases can be studied: the uniaxial compression test with $\Sigma_{rr} = 0$ and the isotropic compression test with $\Sigma_{zz} = \Sigma_{rr}$. In all this section, the classical soil mechanics convention is adopted, i.e. compression stresses are positive, and the elasticity of snow is neglected.
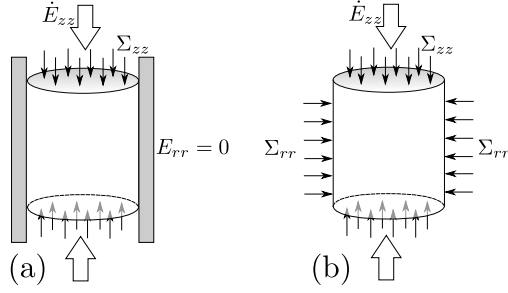
Figure 9. Oedometric compression test (a) and triaxial compression test (b).

5.1 Oedometric compression test

As the snow samples are often extracted from the snowpack thanks to hollow cylinders, the oedometric compression test is one of the most convenient mechanical laboratory test to perform on snow. Under the lateral constraint $E_{rr} = 0$, we have

$$
\dot{\boldsymbol{E}} = \begin{pmatrix} 0 & 0 & 0 \\ 0 & 0 & 0 \\ 0 & 0 & \dot{E}_{zz} \end{pmatrix}. \tag{36}
$$

5   The static equilibrium $\mathrm{div}\,\boldsymbol{\Sigma} = 0$ implies that $\Sigma_{\theta\theta} = \Sigma_{rr}$. Consequently, the macroscopic stress tensor is written

$$
\boldsymbol{\Sigma} = \begin{pmatrix} \Sigma_{rr} & 0 & 0 \\ 0 & \Sigma_{rr} & 0 \\ 0 & 0 & \Sigma_{zz} \end{pmatrix}. \tag{37}
$$

As a result, the two first strain rate and stress invariants are written

$$
E_1 = \dot{E}_{zz}, \qquad \bar{E}_2 = \sqrt{\frac{2}{3}}\dot{E}_{zz}, \qquad S_1 = 2\Sigma_{rr} + \Sigma_{zz}, \qquad \bar{S}_2 = \sqrt{\frac{2}{3}}(\Sigma_{zz} - \Sigma_{rr}), \quad \text{with } \Sigma_{zz} \geq \Sigma_{rr}. \tag{38}
$$

In this particular case, from (33) and (34) it can be shown that the lateral constraint $E_{rr} = 0$ implies that

10   $$
\frac{\Sigma_{rr}}{\Sigma_{zz}} = \frac{c(\phi) - 2f(\phi)}{c(\phi) + 4f(\phi)}, \tag{39}
$$

and consequently,

$$
\Sigma_{\mathrm{eq}} = \sqrt{\frac{9c(\phi)f(\phi)}{4f(\phi) + c(\phi)}}\Sigma_{zz}, \tag{40}
$$

and

$$
\dot{E}_{zz} = A\left(\frac{9f(\phi)c(\phi)}{4f(\phi) + c(\phi)}\right)^{\frac{n+1}{2}}\Sigma_{zz}^n. \tag{41}
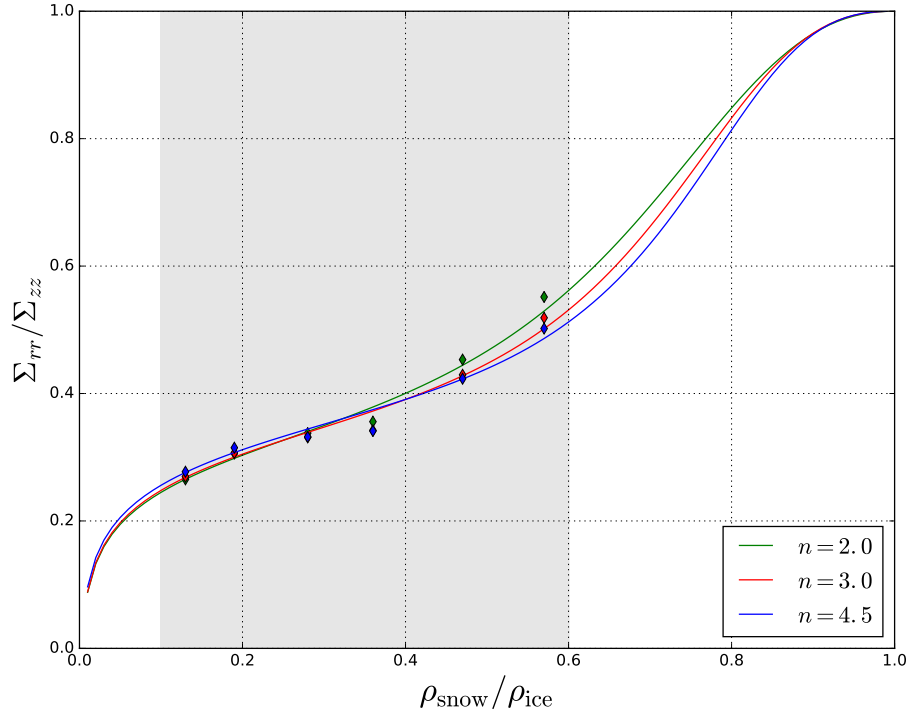$$

Figure 10. Evolution of the ratio between the lateral and axial stresses with respect to snow compacity during any oedometric compression test for different values of the exponent n (numerical points as diamond points, results computed using functions (29) as solid lines). The compacity range for typical snow samples is materialized by the gray zone.

In oedometric experimental tests, the lateral pressure Σ_{rr} is not easily accessible and it is often tempting to neglect this pressure and interpret the oedometric compression test as a uniaxial compression test. The relation (39) can be used to assess the relative importance of the confining pressure with respect to the vertical stress. The evolution of this ratio with respect to snow density is shown in Figure 10 for $n \in \{2, 3, 4.5\}$. It should be noticed that this ratio does not depend on the axial strain rate $\dot{E}_{zz}$. As expected, this ratio increases with increasing snow density, and tends towards one for $\phi = 0$, due to the incompressiblity of the ice skeleton. In the whole range of snow compacities under consideration (materialized by the gray zone in Figure 10) the lateral pressure represents 30 to 50 % of the vertical stress and cannot be neglected in practice. Finally, let us remark that the evolution of this ratio is similar to the one measured by Geindreau et al. (1999a) and Viot and Stutz (2002) on metallic powders. Figure 10 also shows that this ratio is almost independent of the exponent n, which is consistent with the experimental results of Viot and Stutz (2002).

5.2 Triaxial compression test

During a triaxial test, the cylindric snow sample is submitted simultaneaously to an axial stress Σ_{zz} and a lateral confining pressure Σ_{rr}. The static equilbrium $\text{div}\Sigma = 0$ implies that $\Sigma_{\theta\theta} = \Sigma_{rr}$, consequently the macroscopic stress tensor is written

$$\Sigma = \begin{pmatrix} \Sigma_{rr} & 0 & 0 \\ 0 & \Sigma_{rr} & 0 \\ 0 & 0 & \Sigma_{zz} \end{pmatrix}, \tag{42}$$

In these conditions, the constitutive equation (33) implies that $\dot{E}_{\theta\theta} = \dot{E}_{rr}$, and thus

$$\dot{E} = \begin{pmatrix} \dot{E}_{rr} & 0 & 0 \\ 0 & \dot{E}_{rr} & 0 \\ 0 & 0 & \dot{E}_{zz} \end{pmatrix}, \tag{43}$$

As a result, the two first strain rate and stress invariants are written

$$E_1 = 2\dot{E}_{rr} + \dot{E}_{zz}, \qquad \bar{E}_2 = \sqrt{\frac{2}{3}}(\dot{E}_{zz} - \dot{E}_{rr}), \qquad S_1 = 2\Sigma_{rr} + \Sigma_{zz}, \qquad \bar{S}_2 = \sqrt{\frac{2}{3}}|\Sigma_{zz} - \Sigma_{rr}|. \tag{44}$$

In this particular case, from (33) and (34) it can be shown that:

$$\Sigma_{\text{eq}} = \sqrt{f(\phi)(2\Sigma_{rr} + \Sigma_{zz})^2 + c(\phi)(\Sigma_{zz} - \Sigma_{rr})^2}. \tag{45}$$

and

$$\begin{cases} \dot{E}_{rr} = A\Sigma_{\text{eq}}^{n-1}\left[\left(2f(\phi) + \frac{1}{2}c(\phi)\right)\Sigma_{rr} + \left(f(\phi) - \frac{1}{2}c(\phi)\right)\Sigma_{zz}\right] \\ \dot{E}_{zz} = A\Sigma_{\text{eq}}^{n-1}\left[(2f(\phi) - c(\phi))\Sigma_{rr} + (f(\phi) + c(\phi))\Sigma_{zz}\right] \end{cases}. \tag{46}$$

In the case of an uniaxial compression test, Σ_{rr} must be set to 0 in the above equations.

In order to compare the mechanical response of snow under various loadings (uniaxial, oedometric, isotropic and triaxial tests), Figure 11 presents the evolution of the snow densification rate (for $n = 4.5$ and $A = 1.5 \ 10^{-3}\,\text{MPa}^{-n}.\text{s}^{-1}$) given by $E_1 = \dot{\rho}_{\text{snow}}/\rho_{\text{snow}}$ with respect to snow compacity when constant stresses are applied on the sample. As expected, this figure shows that:

– whatever the loading, the densification rate strongly decreases with increasing snow density. In the investigated range, i.e. $\rho_{\text{snow}}/\rho_{\text{ice}} \in [0.1, 0.6]$, the densification rate decreases by 9 orders of magnitude from 10^{-1}s^{-1} to 10^{-10}s^{-1}.

– for a given snow density, the loading conditions influence strongly the densification rate. Typically, when $\Sigma_{zz} = 10$ kPa the densification rate decreases by nearly one order of magnitude if the confining pressure Σ_{rr} is reduced from 10 kPa (isotropic compression) to 0 kPa (uniaxial compression). On the contrary, when $\Sigma_{rr} = 10$ kPa, the densification rate increases by nearly one order of magnitude if the axial stress Σ_{zz} increases from 10 kPa (isotropic compression)
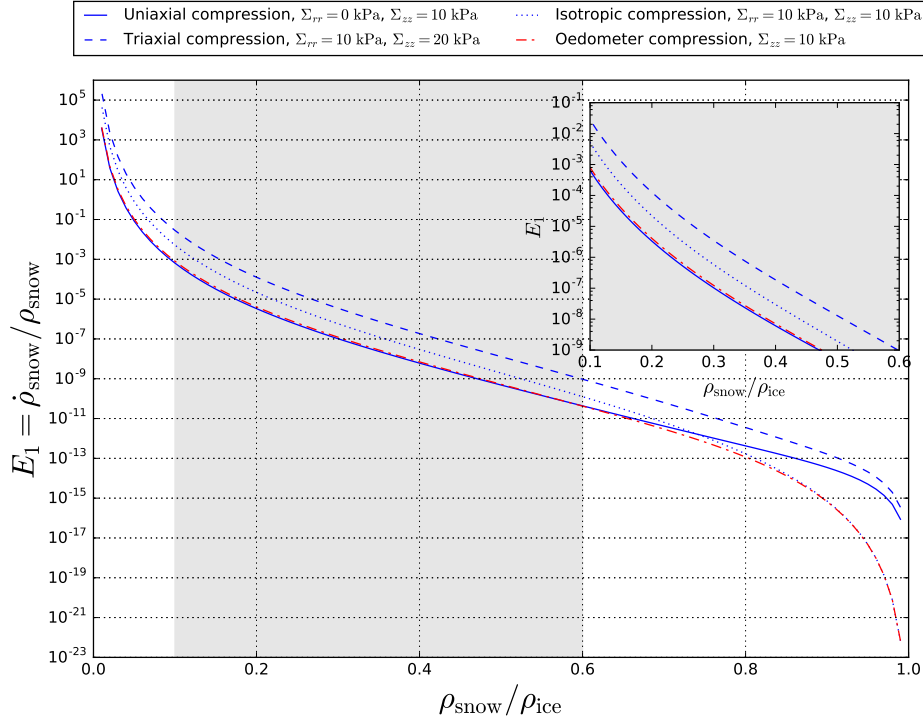
Figure 11. Predicted densification rate (for $n = 4.5$ and $A = 1.5 \ 10^{-3} \, \text{MPa}^{-n}.\text{s}^{-1}$) with respect to snow compacity for four classical laboratory tests: an oedometric compression test (dash-dotted line), a uniaxial compression test (solid line), a triaxial compression test (dashed line) and an isotropic compression test (dotted line). The inset plot provides a zoom on the classical range of snow densities observed experimentally (gray background).

to 20 kPa (triaxial compression). As expected, this last result shows the increase in the densification rate with the increase in the deviatoric stress (i.e. $\bar{S}_2$). Even if the lateral confining pressure cannot be neglected during oedometric test as highlighted in Figure 10, the oedometric compression test results in a similar densification rate as the uniaxial compression test for the same axial stress Σ_{zz}. Indeed, the vertical strain rate is lower for an oedometric compression than for a uniaxial one but the geometrical constraint imposed in the oedometric compression test prevents the snow sample from dilating, which is not the case for the uniaxial compression test. Overall the two effects cancel out each other. Finally, above the classical snow compacity range ($\rho_{\text{snow}}/\rho_{\text{ice}} \geq 0.6$), the densification rate dramatically decreases for the oedometric and isotropic compression tests due to the ice incompressibility. As already underlined in Figure 10, in this limit case, the oedometric compression test is equivalent to the isotropic compression one.

10 In practice, the strain rate is often imposed on the sample. The Figure 12 presents the evolution of the stress Σ_{zz} versus snow compacity $\rho_{\text{snow}}/\rho_{\text{ice}} = 1 - \phi$ for two different values of strain rates $\dot{E}_{zz} \in \{10^{-7}; 10^{-5}\} \, \text{s}^{-1}$ and the different loading conditions (uniaxial, oedometric, isotropic and triaxial tests). This figure suggests the following comments:
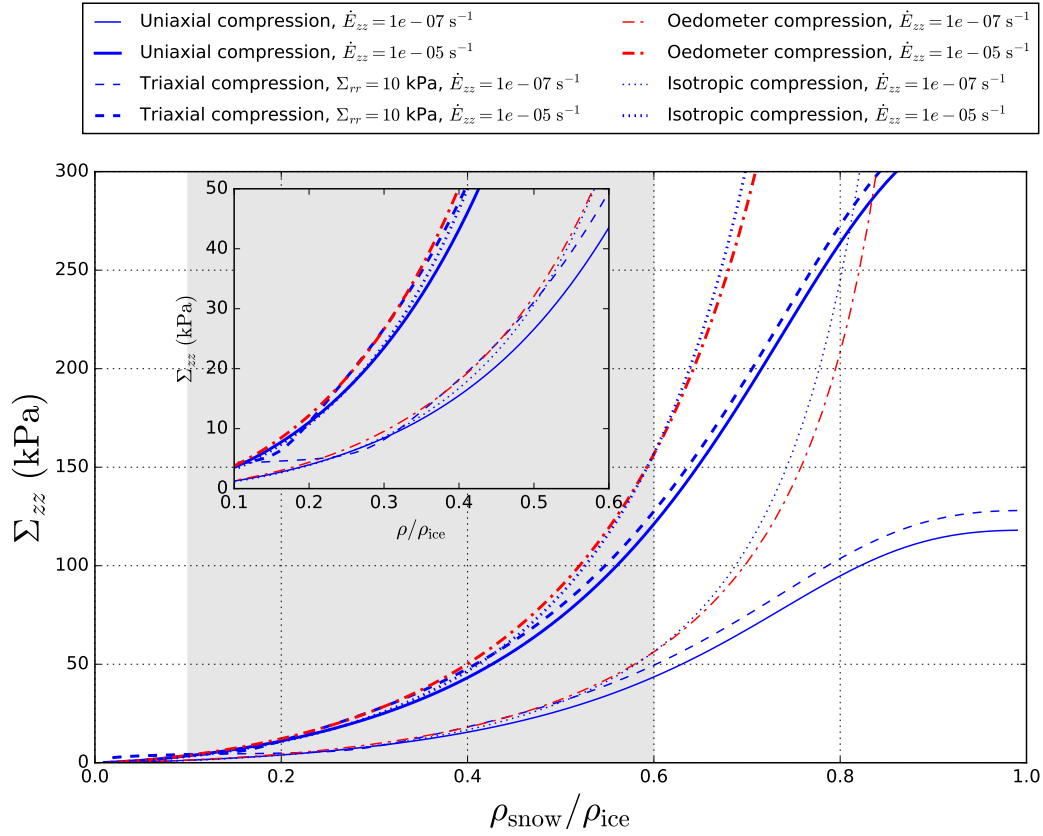
24

Figure 12. Predicted axial stress level (for $n = 4.5$ and $A = 1.5\ 10^{-3}\ \mathrm{MPa}^{-n}.\mathrm{s}^{-1}$) with respect to snow compacity for two imposed strain rates (line thickness) and for four classical laboratory tests: an oedometric compression test (dash-dotted line), a uniaxial compression test (solid line), a triaxial compression test (dashed line) and an isotropic compression test (dotted line). The inset plot provides a zoom on the classical range of snow densities observed experimentally (gray background).

– as expected, for a given strain rate, the stress Σ_{zz} increases with increasing snow density.

– for a given strain rate and a given density, the stress Σ_{zz} increases with increasing the lateral pressure Σ_{rr} around the sample.

– for a given snow density, the stress Σ_{zz} strongly increases with increasing strain rate, which is in accordance with the power law relationship.

– the ice viscoplastic behavior is recovered when $\rho_{\mathrm{snow}}/\rho_{\mathrm{ice}}$ tends towards 1. For a given strain rate, the axial stress for a uniaxial or triaxial compression test tends towards a maximum value. By contrast, due to the incompressibility of ice, the axial stress Σ_{zz} tends towards $+\infty$.

In order to quantitatively compare the predictions of our model against the experimental results of Bartelt and von Moos (2000), we consider a snow of density $\rho_{\text{snow}} = 255$ kg.m^{-3} (corresponding to $\rho_{\text{snow}}/\rho_{\text{ice}} = 0.27$) subjected to a confining pressure of $\Sigma_{rr} = 2.5$ kPa and a strain rate of 2.2×10^{-5} s^{-1}. In this case, the axial stress predicted by our model is $\Sigma_{zz} = 22.8$ kPa, which is consistent with the experimental values obtained by Bartelt and von Moos (2000) around 30 kPa.

5 Further comparison with Bartelt and von Moos (2000) can be achieved in the case of the uniaxial compression test ($\Sigma_{rr} = 0$). In this case, the axial stress simply reads

$$\Sigma_{zz}(\dot{E}_{zz}, \phi) = \left(\frac{\dot{E}_{zz}}{A(f(\phi) + c(\phi))^{\frac{n+1}{2}}} \right)^{\frac{1}{n}}. \tag{47}$$

For a given strain rate, the mechanical response of snow can be compared to the one of ice as in Bartelt and von Moos (2000) by using the following parameter:

10 $$\alpha_\eta(\phi) = \frac{\Sigma_{zz}^{\text{snow}}}{(1-\phi)\Sigma_{zz}^{\text{ice}}} = \frac{\Sigma_{zz}(\dot{E}_{zz}, \phi)}{(1-\phi)\Sigma_{zz}(\dot{E}_{zz}, 0)} = \frac{1}{1-\phi} \left(\frac{1}{f(\phi) + c(\phi)} \right)^{\frac{n+1}{2n}}. \tag{48}$$

This parameter compares the axial stress that a given snow sample can transmit ($\Sigma_{zz}^{\text{snow}}$) to a rough estimate of this stress given as a fraction of the axial stress transmitted in the case of ice ($(1-\phi)\Sigma_{zz}^{\text{ice}}$). In Figure 13, the above theoretical expression of $\alpha_\eta(\phi)$ is compared with the experimental fit $\alpha_\eta = 0.0028 \exp(0.008\rho_{\text{ice}} * (1 - \phi))$ proposed by Bartelt and von Moos (2000). As expected, $\alpha_\eta(\phi)$ increases with increasing snow density. By definition, $\alpha_\eta(\phi)$ should vary between 0 and 1. We

15 can observe that the theoretical expression of $\alpha_\eta(\phi)$ is strictly greater than 1 for $\rho_{\text{snow}}/\rho_{\text{ice}} \in [0.8, 1]$, which is not physically reasonable. This feature results from the independent choices of the parameters a, b, p and q in the fitting procedure used in subsection 4.2. An implicit relation between these parameters could help in order to ensure that $\alpha_\eta(\phi)$ remains lower than 1 in the whole compacity range. Nevertheless, in the range of snow densities under consideration ($\rho_{\text{snow}}/\rho_{\text{ice}} \in [0.1, 0.6]$), α_η increases monotonously between roughly 0.1 and 0.6. This prediction is higher than the experimental fit proposed by Bartelt

20 and von Moos (2000) (see Figure 13). However, during this experiment, the macroscopic mechanical response probably results from both the viscous deformation of the ice skeleton and numerous ruptures of ice bridges between snow grains. Even if our model is able to account for some microstructure modifications through the porosity dependence of the parameters f and c, the changes induced by the experimental testing conditions might exceed the scope of application of our model.

6   Conclusions

25 Despite the non-linearity of the ice viscous constitutive equation, the image-based homogenization approach introduced by Wautier et al. (2015) was successfully adapted to the numerical homogenization of snow viscous behavior. It allows the viscoplastic response of any snow sample being computed from its X-ray tomographic image. By contrast to the elastic case, the macroscopic stress response is not a linear function of the imposed macroscopic strain anymore. As a result, the macroscopic response of snow was investigated in terms of isodissipation curves in the planes of the two first strain rate and stress invari-

30 ants. The shape and size of these curves characterize the strong coupling between the snow microstructure and the ice viscous
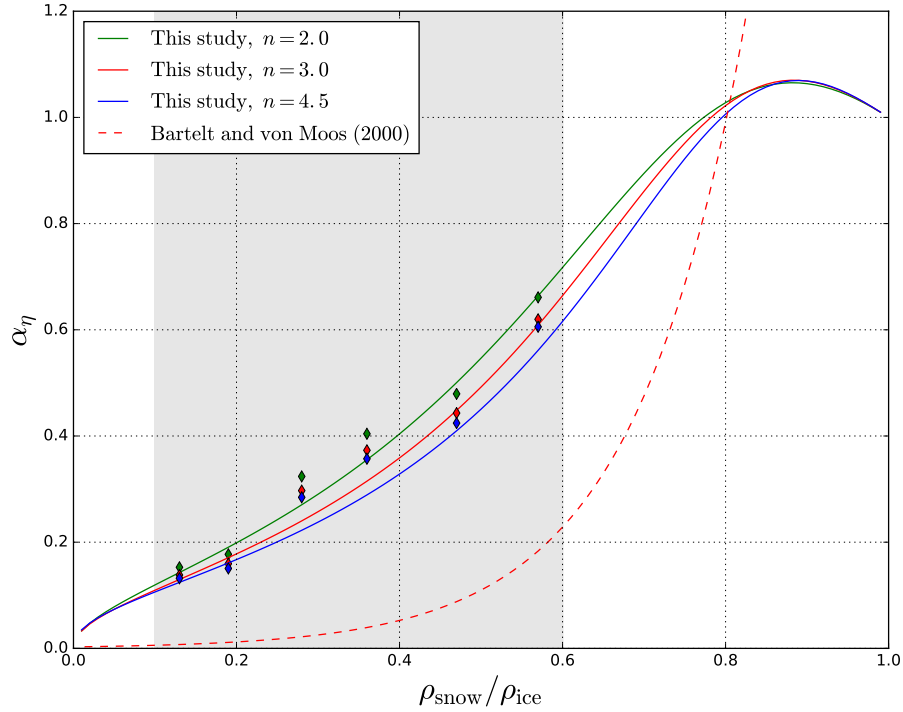
Figure 13. Comparison between our theoretical prediction for α_η (48) and the experimental fit proposed by Bartelt and von Moos (2000). The points computed directly from the values for f and c reported in Table 3 are shown as diamond points. The compacity range for snow samples under consideration is materialized by the gray zone.

behavior (power law with an exponent n) at the microscopic scale. Different values for n were considered in this study to give some insight on their influence on the homogenized viscoplastic behavior of snow. Thanks to a few selected loading paths, an Abouaf's model was fitted onto the numerical results. This formulation seems to be relevant to describe the snow viscoplastic behavior in the whole range of snow density under consideration ($0.43 < \phi < 0.87$), provided that the snow microstructure is isotropic. For a given value of n, the influence of the snow microstructure, on the viscoplastic response of snow is described at the first order through two materials functions ($f(\phi)$ and $c(\phi)$, see (29)) which depend on the porosity only.

The robustness of this Abouaf formulation is tested for several isotropic snow samples covering the whole range of accessible densities. The fitted models proved to be able to account for the stress and strain rate levels as well as the viscous flow directions. In particular and contrary to the case of ice, the ability of snow to exhibit a viscous behavior even under isotropic strain loading is recovered. The scope of application of the presented unified formulation is quite promising and could help improve the modeling of the densification of the snowpack in avalanche forecasting models.

The proposed homogenization model can be easily used to predict the viscous behavior of snow in classical laboratory tests as illustrated in the last section of this paper. However, the uncertainties made on our model parameters should be quantified

through a sensitivity analysis, in order to reckon the ability of our homogenized law for snow viscosity to quantitatively recover the experimental results of Desrues et al. (1980); Bartelt and von Moos (2000); Moos et al. (2003); Scopozza and Bartelt (2003b).

Even though the porosity is known to have a very strong influence on the resulting homogenized properties of snow, it is also acknowledged that the very strong anisotropy of some snow microstructures cannot be neglected. The importance of this anisotropy was quantified within the framework of elasticity (Srivastava et al., 2010, 2016; Wautier et al., 2015) but the extension of our homogenized visco-plastic formulation to anisotropic snow types is quite challenging as the dimension of the invariant space will increase dramatically (Boehler, 1978; Liu, 1982; Hansen et al., 1991).

Finally, in the present work based on FEM simulations, the ice skeleton is viewed as a continuous polycrystalline material. The proposed methodology to identify and formulate the 3D viscoplastic behavior of snow can be also applied to DEM simulations. For that purpose, the identification of the shape and crystalline orientations of every ice grain (Rolland du Roscoat et al., 2011) as well as the knowledge of the viscoplastic contact laws (Burr et al., 2015b, a) would be of primary interest.

References

Abouaf, M.: Modélisation de la compaction de poudres métalliques frittées, Ph.D. thesis, 1985.

Abouaf, M. and Chenot, J.: Finite element simulation of hot isostatic pressing of metal powders, Int. J. for Num. Meth. in Eng., 25, 191–212, 1988.

Adams, E. E. and Walters, D. J.: Fine structure layering in radiation recrystallized snow, in: International Snow Science Workshop 2014 Proceedings, Banff, Canada, pp. 29–34, ISSW, 2014.

Auriault, J.-L., Bouvard, D., Dellis, C., and Lafer, M.: Modeling of hot compaction of metal powder by homogenization, Mech. Mater., 13, 247–275, 1992.

Auriault, J.-L., Royer, P., and Geindreau, C.: Filtration law for power law fluids in anisotropic media, Int. J. Eng. Sc., 40, 1151–1163, 2002.

Auriault, J.-L., Boutin, C., and Geindreau, C.: Homogenization of coupled phenomena in heterogenous media, vol. 149, John Wiley & Sons, 2010.

Bartelt, P. and von Moos, M.: Triaxial tests to determine a microstructure-based snow viscosity law, Annals of Glaciology, 31, 457–462, 2000.

Boehler, J.: Lois de comportement anisotrope des milieux continus, Journal de mécanique, 17, 153–190, 1978.

Brzoska, J.-B., Coléou, C., Lesaffre, B., Borel, S., Brissaud, O., Ludwig, W., Boller, E., and Baruchel, J.: 3D visualization of snow samples by microtomography at low temperature, ESRF Newsletter, 32, 22–23, 1999.

Burr, A., Philip, A., and Martin, C.: Etude expérimentale de la déformation viscoplastique de cylindres monocristallins de glace, in: Plasticité 2015, Autrans, 28-30 avril, 2015a.

Burr, A., Trecourt, P., Philip, A., and Martin, C.: Densification of firn using the Discrete Element Method, in: ESMC 2015, 9th European Solid Mechanics Conference, Madrid 6-10 July, 2015b.

Calonne, N., Geindreau, C., Flin, F., Morin, S., Lesaffre, B., Rolland du Roscoat, S., and Charrier, P.: 3-D image-based numerical computations of snow permeability: links to specific surface area, density, and microstructural anisotropy, The Cryosphere, 6, 939–951, doi:10.5194/tc-6-939-2012, 2012.

Calonne, N., Flin, F., Geindreau, C., Lesaffre, B., and Rolland du Roscoat, S.: Study of a temperature gradient metamorphism of snow from 3-D images: time evolution of microstructures, physical properties and their associated anisotropy, The Cryosphere, 8, 2255–2274, 2014.

Calonne, N., Flin, F., Lesaffre, B., Dufour, A., Roulle, J., Puglièse, P., Philip, A., Lahoucine, F., Geindreau, C., Panel, J.-M., Rolland du Roscoat, S., and Charrier, P.: CellDyM: A room temperature operating cryogenic cell for the dynamic monitoring of snow metamorphism by time-lapse X-ray microtomography, Geophysical Research Letters, 42, 3911–3918, doi:10.1002/2015GL063541, 2015.

Chandel, C., Srivastava, P. K., and Mahajan, P.: Micromechanical analysis of deformation of snow using X-ray tomography, Cold Regions Science and Technology, 101, 14–23, 2014.

Chen, S. and Baker, I.: Evolution of individual snowflakes during metamorphism, J. Geophys. Res., 115, D21114, doi:10.1029/2010JD014132, 2010.

Cresseri, S. and Jommi, C.: Snow as elastic viscoplastic bonded continuum: a modelling approach, Rivista Italiana Di Geotecnica, 4, 43–58, 2005.

Cresseri, S., Genna, F., and Jommi, C.: Numerical integration of an elastic-viscoplastic constitutive model for dry metamorphosed snow, Int. J. Num. Ana. Meth. Geomech, 34, 1271–1296, 2009.

Danas, K., Idiart, M., and Ponte Casteneda, P.: A homogenization-based constitutive model for isotropic viscoplastic porous media, Int. J. Solids and Struct., 45, 3392–3409, 2008.

Desrues, J., Darve, F., Flavigny, E., Navarre, J., and Taillefer, A.: An incremental formulation of constitutive equations for deposited snow, Journal of Glaciology, 25, 289–307, 1980.

5 Dormieux, L. and Bourgeois, E.: Introduction à la micromécanique des milieux poreux, Presses de l'École nationale des ponts et chaussées, 2002.

Duva, J. and Crow, P.: The densification of powders by power-law creep during hot isostatic pressing, Acta Metall Mater., 40, 31–35, 1992.

Fang, Q. and Boas, D. A.: Tetrahedral mesh generation from volumetric binary and grayscale images, in: Biomedical Imaging: From Nano to Macro, 2009. ISBI'09. IEEE International Symposium on, pp. 1142–1145, IEEE, http://iso2mesh.sourceforge.net/cgi-bin/index.cgi,

10 2009.

Fierz, C., Armstrong, R. L., Durand, Y., Etchevers, P., Greene, E., McClung, D. M., Nishimura, K., Satyawali, P. K., and Sokratov, S. A.: The International Classification for Seasonal Snow on the Groung, UNESCO/IHP, 2009.

Flin, F. and Brzoska, J.-B.: The temperature-gradient metamorphism of snow: vapour diffusion model and application to tomographic images, Annals of Glaciology, 49, 17–21, 2008.

15 Fritzen, F., Forest, S., Bohlke, T., Kondo, D., and Kanit, T.: Computational homogenization of elasto-plastic porous metals, Int. J. of Plasticity, 29, 102–119, 2012.

Geindreau, C. and Auriault, J.-L.: Investigation of the mechanical behaviour of alloys in the semi-solid state by homogenization., Mechanics of Materials, 31, 535–551, 1999.

Geindreau, C., Bouvard, D., and Doremus, P.: Constitutive behaviour of metal powder during hot forming. Part I : experimental investigation

20 with lead powder as a simulation material, Eur. J. Mech. A/Solids, 18, 581–596, 1999a.

Geindreau, C., Bouvard, D., and Doremus, P.: Constitutive behaviour of metal powder during hot forming.: Part II: Unified viscoplastic modelling, European Journal of Mechanics-A/Solids, 18, 597–615, 1999b.

Green, R.: A plasticity theory for porous solids, International Journal of Mechanical Sciences, 14, 215–224, 1972.

Hagenmuller, P., Theile, T. C., and Schneebeli, M.: Numerical simulation of microstructural damage and tensile strength of snow, Geophys.

25 Res. Lett., 41, 86–89, doi:10.1002/2013GL058078, 2014.

Hagenmuller, P., Chambon, G., and Naaim, M.: Microstructure-based modeling of snow mechanics: a discrete element approach, Cryosphere, 9, 1969–1982, 2015.

Hansen, A. C., Blackketter, D. M., and Walrath, D. E.: An invariant-based flow rule for anisotropic plasticity applied to composite materials, Journal of Applied Mechanics, 58, 881, 1991.

30 Johnson, J. B. and Hopkins, M. A.: Identifying microstructural deformation mechanisms in snow using discrete element modeling, Journal of glaciology, 51, 2005.

Kaempfer, T. U., Schneebeli, M., and Sokratov, S.: A microstructural approach to model heat transfer in snow, Geophysical Research Letters, 32, 2005.

Kanit, T., Forest, S., Galliet, I., Mounoury, V., and Jeulin, D.: Determination of the size of the representative volume element for random

35 composites: statistical and numerical approach, International Journal of solids and structures, 40, 3647–3679, 2003.

Köchle, B. and Schneebeli, M.: Three-dimensional microstructure and numerical calculation of elastic properties of alpine snow with a focus on weak layers, Journal of Glaciology, 60, 705–713, 2014.

Lejeunes, S., Bourgeois, S., et al.: Une Toolbox Abaqus pour le calcul de propriétés effectives de milieux hétérogènes, in: 10e colloque national en calcul des structures, http://www.lma.cnrs-mrs.fr/spip.php?article171, 2011.

Lemaitre, J. and Chaboche, J.-L.: Mécanique des Matériaux Solides, Dunod, Paris, 1985.

Liu, I.-S.: On representations of anisotropic invariants, International Journal of Engineering Science, 20, 1099–1109, 1982.

5   Löwe, H., Riche, F., and Schneebeli, M.: A general treatment of snow microstructure exemplified by an improved relation for thermal conductivity, The Cryosphere, 7, 1473–1480, doi:10.5194/tc-7-1473-2013, 2013.

Mellor, M.: A review of basic snow mechanics, US Army Cold Regions Research and Engineering Laboratory, 1974.

Moos, M. v., Bartelt, P. A., Zweidler, A., and Bleiker, E.: Triaxial tests on snow at low strain rate. Part I: Experimental device, Journal of Glaciology, 49, 81–90, 2003.

10 Narita, H.: An experimental study on tensile fracture of snow, Contributions from the institute of Low Temperature Science, 32, 1–37, 1984.

Navarre, J. P., Meyssonnier, J., and Vagnon, A.: 3D numerical model of snow deformation without failure and its application to cold room mechanical tests, Cold Regions Science and Technology, 50, 3–12, 2007.

Orgéas, L., Geindreau, C., Auriault, J.-L., and Bloch, J.-F.: Upscaling the flow of generalised Newtonian fluids through anisotropic porous media, Journal of Non-Newtonian Fluid Mechanics, 145, 15–29, 2007.

15 Pieritz, R. A., Brzoska, J.-B., Flin, F., Lesaffre, B., and Coléou, C.: From snow X-ray microtomograph raw volume data to micromechanics modeling: first results, Ann. Glaciol., 38, 52–58, doi:10.3189/172756404781815176, 2004.

Pinzer, B., Schneebeli, M., and Kaempfer, T.: Vapor flux and recrystallization during dry snow metamorphism under a steady temperature gradient as observed by time-lapse micro-tomography, The Cryosphere Discussions, 6, 1673–1714, 2012.

Rolland du Roscoat, S., King, S., Philip, A., Reischig, A., Ludwig, P., Flin, F., and Meysonnier, J.: Analysis of snow microstructure by means
20 of X-ray diffraction contrast tomography, Advanced Engineering Materials, 13, 128–135, 2011.

Salm, B.: Mechanical properties of snow, Rev. Geophys., 20, 1–19, 1982.

Sanchez, L., Ouedraogo, E., Federzoni, L., and Stutz, P.: New viscoplastic model to simulate hot isostatic pressing, Powder metallurgy, 45, 329–334, 2002.

Scapozza, C. and Bartelt, P.: Triaxial tests on snow at low strain rate. Part II. Constitutive behaviour, Journal of Glaciology, 49, 91–101, 2003.

25 Schleef, S., Löwe, H., and Schneebeli, M.: Hot-pressure sintering of low-density snow analyzed by X-ray microtomography and in situ microcompression, Acta Materialia, 71, 185–194, 2014.

Schneebeli, M.: Numerical simulation of elastic stress in the microstructure of snow, Annals of Glaciology, 38, 339–342, 2004.

Schulson, E. M., Duval, P., et al.: Creep and fracture of ice, Cambridge University Press Cambridge, 2009.

Schweizer, J. and Camponovo, C.: The temperature dependence of the effective elastic shear modulus of snow, Cold Regions Science and
30 Technology, 35, 55–64, 2002.

Scopozza, C. and Bartelt, P. A.: The influence of temperature on the small strain viscous deformation mechanics of snow: comparison with polycrystalline ice, Annals of Glaciology, 37, 90–96, 2003a.

Scopozza, C. and Bartelt, P. A.: Triaxial tests on snow at low strain rate. Part II: Constitutive modelling, Journal of Glaciology, 49, 91–101, 2003b.

35 Shapiro, L. H., Johnson, J. B., Sturm, M., and Blaisdell, G. L.: Snow mechanics: review of the state of knowledge and applications, 1997.

Smith, G.: On Isotropic Functions of Symmetric Tensors Skew-Symmetric Tensors and Vectors, Int. J. Eng. Sci., 9, 899–916, 1971.

Sofronis, P. and McMeecking, R.: Creep of power-law material containing spherical voids, Journal of Applied Mechanics, 59, S88–S95, 1992.

Srivastava, P., Mahajan, P., Satyawali, P., and Kumar, V.: Observation of temperature gradient metamorphism in snow by X-ray computed microtomography: measurement of microstructure parameters and simulation of linear elastic properties, Annals of Glaciology, 51, 73–82, 2010.

Srivastava, P. K., Chandel, C., Mahajan, P., and Pankaj, P.: Prediction of anisotropic elastic properties of snow from its microstructure, Cold Regions Science and Technology, 125, 85–100, 2016.

Storakers, B., Fleck, N. A., and McMeeking, R. M.: The viscoplastic compaction of composite powders, J. Mech. Phys. Solids, 47, 785–815, 1999.

Suquet, P.: Overall potentials and extremal surfaces of power law or ideally plastic composites, Journal of the Mechanics and Physics of Solids, 41, 981–1002, 1993.

Theile, T., Lowe, H., Theile, T. C., and Schneebeli, M.: Simulating creep of snow based on microstructure and anisotropic deformation of ice, Acta Materialia, 59, 7104–7113, 2011.

Viot, P. and Stutz, P.: Nouveau dispositif expérimental pour l'étude du comportement viscoplastique des poudres métalliques à hautes températures : application à une poudre de cuivre, C. R. Mecanique., 330, 653–659, 2002.

Wang, X. and Baker, I.: Observation of the microstructural evolution of snow under uniaxial compression using X-ray computed microtomography, Journal of Geophysical Research: Atmospheres, 118, 12–371, 2013.

Wautier, A., Geindreau, C., and Flin, F.: Linking snow microstructure to its macroscopic elastic stiffness tensor: A numerical homogenization method and its application to 3-D images from X-ray tomography, Geophysical Research Letters, 42, 8031–8041, 2015.